The Electrochemical Properties of Iron Diselenide Hedgehog Particles

by

Yuan Cao

A dissertation submitted in partial fulfillment
of the requirements for the degree of
Doctor of Philosophy
(Chemical Engineering)
in the University of Michigan
2022

Doctoral Committee:

Professor Nicholas A. Kotov, Chair
Professor Jinsang Kim
Professor Johannes W. Schwank
Assistant Professor Nirala Singh

Yuan Cao

yuancao@umich.edu

ORCID iD: 0000-0002-3544-2664

Dedication

I would like to dedicate this dissertation to my parents and my family.

Acknowledgements

First of all, I would like to sincerely thank Prof. Nicholas A. Kotov. Thank you for taking me as your graduate student back in September 2018. Three and a half year does not seem too long, but I definitely learned a lot since then, especially knowledge in the nanoscale world and experience working with many material characterization tools. I could not finish this degree without your continuous support and trust. You are a wonderful person who always believe in me even in many toughest moments. You are a role model that I always look up to and I will try my best to keep in mind to be different when I leave the school and step into the industrial world.

Next, I also would like to extend my great appreciation to other members in my dissertation committee – Prof. Jinsang Kim, Prof. Nirala Singh, and Prof. Johannes W. Schwank – for your kind help and guidance on my research project and dissertation.

Then, I want to say thank to my first advisor Prof. Mark A. Barteau. I greatly appreciated that you picked me as your graduate student in 2016. Although things did not turn out as we planned, I still feel grateful for your continuous help towards completing the polyoxometalate project with a full article and an oral presentation. I also want to express my appreciation to my second advisor Prof. Levi T. Thompson for your courage and determination. There are certain things we cannot control, but I would like to thank you for many great suggestions and advices along the way.

I want to express my gratitude to members in the Barteau research group, the Thompson research group, and the Kotov lab. Specifically Dr. Xiaowen Zhao and Dr. Jee-jay James Chen from the Barteau research group; Yixuan Chen and Dr. Saemin Choi from the Thompson research

group; Elizabeth Wilson, Connor McGlothin, Dr. Jun Lu, Xiao Shao and Chung-Man Lim from the Kotov Lab for mentoring, solving my problems, answering my questions, giving me support, and collaborating together as teams. Furthermore, I would like to say thank to my collaborator Dr. Bingcheng Luo in this dissertation project for performing the computational work.

I have to thank my family and friends as well. My parents are always so supportive no matter what decisions I made. You gave me a strong faith to complete my Ph.D. degree, which is the hardest thing in the world. I am blessed because I was loved by you. Besides, there are too many friends to list out whom I want to express my thankfulness with their support mentally. It is always good to have Ph.D. fellow to share opinions and feelings together.

The funding source of this dissertation project is from Vannevar Bush Department of Defense (DoD) Fellowship to Prof. Nicholas A. Kotov. The central part of this work was supported by the National Science Foundation (NSF), and the Office of Naval Research (ONR) COVID-19 Newton Award are also gratefully acknowledged. I also acknowledge the technical support from the Michigan Center for Materials Characterization ($(MC)^2$).

Table of Contents

List of Tables

List of Figures

List of Abbreviations

CV	Cyclic Voltammetry / Cyclic Voltammogram
DC	Direct Current
DFPT	Density Functional Perturbation Theory
DLS	Dynamic Light Scattering
DMF	*N,N*-dimethylformamide
DMSO	Dimethyl Sulfoxide
ECSA	Electrochemically Active Surface Area
EIS	Electrochemical Impedance Spectroscopy
Fc/Fc^+	Ferrocene (Fc) / Ferrocenium (Fc^+)
GCWE	Glassy Carbon Working Electrode
GGA	Generalized Gradient Approximation
HER	Hydrogen Evolution Reaction
HP	Hedgehog Particle(s)
LiTf	Lithium Trifluoromethanesulfonate
LSV	Linear Sweep Voltammetry / Linear Sweep Voltammogram
$(MC)^2$	Michigan Center for Materials Characterization
NP(s)	Nanoparticle(s)
NTA	Nanoparticle Tracking Analysis
OCP	Open Circuit Potential
OER	Oxygen Evolution Reaction

QD	Quantum Dots
Quasi	Quasireversible
RDE	Rotating Disk Electrode
R_u	Uncompensated Resistance
RVC	Reticulated Vitreous Carbon
SEM	Scanning Electron Microscopy
SERS	Surface-Enhanced Raman Scattering
TBA	Tetrabutylammonium
TBAP	Tetrabutylammonium Perchlorate
$TBAPF_6$	Tetrabutylammonium Hexafluorophosphate
THAP	Tetrahexylammonium Perchlorate
UV-Vis	Ultraviolet-Visible Spectroscopy
XPS	X-ray Photoelectron Spectroscopy

Abstract

The exceptional charging capacity of colloidal semiconductor nanoparticles has garnered increasing attention from some researchers. This dissertation aims to expand the charging capacity from nanoparticles to nanoparticle assemblies, focusing on utilizing the high surface corrugation and complex geometric features of iron diselenide hedgehog particles ($FeSe_2$ HPs) to understand better their electrochemical properties and find an electrolyte system suitable for further studies. Cyclic Voltammetry (CV) experiments were first performed to select the best combination (solvent, supporting electrolyte, and working electrode) for the electrolyte system to fully utilize the electrochemical activities of $FeSe_2$ HPs. The system of $FeSe_2$ HPs with 0.1 M lithium trifluoromethanesulfonate (LiTf) in *N,N*-dimethylformamide (DMF) using a gold disk working electrode stood out and will be applied for further studies. This electrolyte system was discovered to be electrochemically stable for a long-term CV test up to 4 hours, and the hedgehog structure remained intact throughout the course of the electrochemical experiment. CV of $FeSe_2$ HPs indicated an oxidation peak related to $FeSe_2$, and bulk electrolysis plot along with density functional perturbation theory (DFPT) calculations both demonstrate a high number in the magnitude of 10^8 positive charges stored per single HP, which is the largest number reported to date in the perspective of charging capacity per nanoparticle assemblies. The charging capacity of $FeSe_2$ HPs in this electrolyte system surpassed other previously studied colloidal semiconductor nanoparticles in many aspects including charges per surface area of a single particle, per volume of a single particle, and per crystalline unit cell. X-ray Photoelectron Spectra showed that mostly the selenium atoms will be oxidized during the bulk oxidation of $FeSe_2$ HPs. Due to the great

electrochemical properties of $FeSe_2$ HPs, they have the potential to be utilized as 'dispersed' heterogeneous electrocatalysts in many heterogeneous electrocatalytic systems.

Chapter 1 Introduction

1.1 Nanoparticles in Electrolyte Systems

During the past few decades, colloidal semiconductor nanoparticles (NPs) or quantum dots (QDs) have attracted considerable attention due to their tunable electronic properties as a function of sizes, the quantum size effect.[1] It was known that the optical band gap of semiconductor NPs has a strong dependency with the size. Besides, researchers have found that the value of peak separation obtained by Cyclic Voltammetry (CV) experiments have a strong correlation with the value of optical band gap.[1–7] Haram *et al.* found that the CdS NPs with a diameter range between 3.9 to 4.5 nm have a band gap range from 3.06 to 3.23 eV, which correspond well with the peak separation of 2.63 to 3.39 V obtained by CV test with a scan rate of 100 mV/s.[1] Inamdar *et al.* determined many band structure parameters such as the conduction band edge, the valence band edge and the quasi-particle gap of diffusing CdSe QDs of various sizes were using CVs. These parameters were strongly dependent on the size of the QDs.[5] Haram *et al.* later applied CV as a tool to study the quantum confinement in oleic acid stabilized CdTe QDs dispersions. The band structure parameters have been estimated as a function of QD sizes, ranging from *ca.* 2.4 to 4.7 nm and compared with the corresponding UV-Vis (Ultraviolet-Visible Spectroscopy) data.[3] In a nutshell, this correlation shapes the unique electrochemical properties of these NPs, which can potentially facilitate the application of these NPs in some energy-related fields.

Apart from this correlation through CV experiments, Haram *et al.* did an estimation based on the size and the diffusion coefficient, indicating a passage of *ca.* 50 electrons/particle at the peak potentials,[1] which is a large amount of charge stored for a cadmium sulfide (CdS) NP with a

diameter of around 4 nm. Considering the capacitive effect, about 30 electrons can be deposited on NPs, therefore, around 20 electrons were transferred to each CdS NP due to the chemical reactions.

Albery *et al.* also reported a maximum 270 electrons transferred on each encounter of a 8.0 nm diameter CdS NP with a macroscopic optical rotating disk electrode by adding halide ions, especially bromide ions into the electrolyte system.[8] If an approximation of 125 electrons settled on the surface is taken into account, there are still about 145 electrons stored on the CdS colloidal semiconductor particles owing to the redox processes involving these particles.

Both results look very promising since both NPs displayed a larger charging capacity compared to that as pure electrochemical capacitors while maintaining the structure integrity. Nevertheless, some further questions have been raised. Firstly, can the number of charge storage be further extended if we self-assemble NPs into larger structures with complex geometry? Secondly, will the unique electrochemical properties of colloidal semiconductor NPs apply to their assemblies as well? What would the appropriate methods for their electrochemical studies? These are the questions that I will answer in this dissertation.

1.2 Electrochemistry of Nanoparticle Assemblies

Concurrent studies on electrochemistry of NP assemblies without any surface corrugations has already shown unusual properties of electroactive nanostructures. For example, they have a huge charge storage capacity (section 1.1),[1,8,9] can facilitate (electro)catalysis,[10,11] and exhibit charge-dependent optical effects.[1–3,5,12–14]

However, surface roughness and geometrical features at nanometer scale, are known to affect electrochemical properties of both macroscale electrodes and particle dispersions.[15] For

instance, carbon electrodes with various surface roughness can perform differently in electrochemical measurements.[16] On the other hand, NPs with same chemical composition but different geometrical features, such as nanoslices or nanoplatelets, can have a different electrochemical performances.[17]

There are multiple studies highlighting the role of surface morphology of electroactive particles for charge-discharge performance of batteries[18–21], supercapacitors[17,18], fuel cells[20], and detectors[16]. There is a trend that nanoarchitectures with complex features and higher corrugation tend to enhance the electrochemistry properties. Many areas of technology from energy storage[17–23] and electrocatalysis[24–28] to biosensing[29–33] will benefit from the maximization of charge stored on particles from electroactive materials.

Theoretical calculations and simulations also indicate that electrodes with high aspect roughness have more possibilities of various charge transport anomalies compared to that of classical flat electrodes[34]. Single particle electrochemistry confirms the complexity of coupled structural, charging and mass transport processes on submicron spikes.[35]

Further studies at the nexus of surface corrugations, chemistry and physics of electroactive colloidal particles would also be intriguing because one can expect amplification[36] of anomalous charge dynamics and field concentration effects at the nanoscale apexes.[37–39] Additionally, nanoscale surface features may increase the surface charge density. However, an experimental model to answer these foundational questions along this path, for example, about the limits for charge accumulation and its effects on the chemical structure and optical characteristics of the electroactive material are currently missing. Furthermore, systematic studies of surface corrugation on electrochemical properties of colloidal particles are limited, on one hand, by limitations of top-down manufacturing of nanoelectrodes with high aspect ratios[35], and on the other

hand, by strong tendency of colloidal particles to coagulate[40,41] in electrolytes necessary for electrochemical studies.

Therefore, a study addressing these questions requires carefully designed experimental system combining, surface corrugation with effective electron transport and colloidal stability in different electronic states.

1.3 Hedgehog Particles (HPs)

We hypothesized that hedgehog particles (HPs) coated with high aspect ratio spikes from various materials can address these problems because they resist coagulation in hydrophilic, hydrophobic and high ionic strength media.[42–45]

HPs were introduced about seven years ago by a previous fellow in the Kotov lab. Bahng *et al*. produced micrometer-sized particles that were coated with stiff nanoscale spikes and exhibited long-term colloidal stability in both hydrophilic and hydrophobic media. It was found that these HPs do not interpenetrate each other with their spikes, which markedly decreases the contact area between the particles, and therefore the attractive forces between them. The trapping of air in aqueous dispersions, solvent autoionization at highly developed interfaces, and long-range electrostatic repulsion in organic media all contribute to the colloidal stability of HPs in various dispersions.[42]

Due to the unique properties of HPs, which overturn the notion of 'like dissolves like', they can be applied to various technologies. Montjoy *et al.* had surface-modified HPs with multilayers of polymers and gold NPs, and these HPs are capable of surface-enhanced Raman scattering (SERS) and overcome the limited colloidal stability of other SERS probes. The agglomeration resilience of HPs leads to a greater than one order of magnitude increase of SERS intensity as

compared to colloids with smooth surfaces and enables simultaneous detection of several targets in complex media with high ionic strength.[43]

HPs modified by partial removal or complete removal of zinc oxide (ZnO) nanospikes with nanoscale polymeric spikes (referred as tendril particles), which were made by layer-by-layer assembly of polyallylamine films deposited onto rigid ZnO templates possessed a potential stimuli-responsive behavior. Montjoy *et al.* found that these polymer spikes also allow for loading of cargo nanoparticles, molecules, and polymers. By adding poly(*N*-isopropylacrylamide-*co*-acrylic acid) subunits, controlled aggregation is observed in response to temperature. Structural integration of dopamine moieties into the layered films allows for controlled aggregation in response to alkaline conditions.[44]

Apart from these, HPs can be applied as a photocatalyst for a photocatalytic reaction of lignin model monomer (2-phenoxy-1-phenylethanol with *β*-O-4 bonds) photooxidation, reported by Montjoy *et al.* [45] Cleavage of *β*-O-4 bonds is of particular importance, as they make up 50−60% of all the C−O linkages in lignin.[46] The details will be discussed in Chapter 5.

1.4 Iron Diselenide Hedgehog Particles

Among all these HPs synthesized[42–45,47], $FeSe_2$ HPs synthesized by Deng *et al.*[47] in 2017 stood out as the most promising candidate to be applied in electrolyte systems and investigate their electrochemical properties for two reasons. First of all, $FeSe_2$ is a semiconductor material with a band gap between 0.6 and 1.0 eV from Generalized Gradient Approximation (GGA) calculations (calculated by the collaborator Dr. Bingcheng Luo). So it is more conductive than other materials applied in other HPs. For instance, ZnO as nanospikes has a band gap between 3.1 – 3.3 eV[48], and the core SiO_2 is a complete insulator.

Secondly, $FeSe_2$ HPs have a better structure integrity compared with other HPs with different chemical compositions on the core and the nanospikes (e.g. SiO_2 core and ZnO nanospikes) because the core and nanospikes are both made of $FeSe_2$ (Figure 1-1). In $FeSe_2$ HPs, the diameter of the $FeSe_2$ core is less than 10 nm so it is hidden by the nanospikes. Besides, $FeSe_2$ HPs were synthesized by a template-free one-pot reaction after mixing the selenium dispersion and the iron dispersion. Therefore, the core and nanospikes were simultaneously growing as time went by.[47]

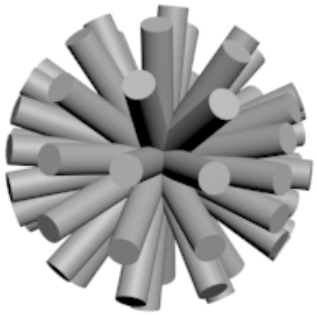

Figure 1-1 $FeSe_2$ HPs made by 3ds Max. © 2022 Yuan Cao

HPs have a highly complex hedgehog structure and large surface corrugation owing to the surface coating with stiff nanospikes. HPs are also omnidispersible, which is highly beneficial as active species in the electrolyte systems. $FeSe_2$ HPs inherit the merits from HPs, along with the semiconductor essence of $FeSe_2$ and a better structure integrity, should be a great candidate among other NPs assemblies to be applied in this dissertation project to study their electrochemical properties.

1.5 Research Goals

The overall research goal of the project presented in this dissertation is to investigate the electrochemical properties of $FeSe_2$ HPs in the electrolyte system. It can be separated into three parts, that is

1. Build a suitable electrolyte system for $FeSe_2$ hedgehog particles
2. Investigate the electrochemical properties of the system
3. Develop energy-related applications for the system

Therefore, this dissertation will be divided into five chapters as outlined below.

1.6 Chapter Summaries

1.6.1 Chapter 1 Introduction

In this chapter, I will give an introduction to the dissertation. Starting with the findings of the huge charging capacity of colloidal semiconductor QDs in the electrolyte systems[1,8], I analyze the reason to potentially further improve the electrochemical performance, *i.e.* to find a nanoscale architecture with high surface corrugation and complex geometric features. Coincidentally, the HPs introduced a few years ago by the Kotov lab[42] satisfied both requirements, and their omni-dispersibility also brings another benefit for electrolyte systems due the drastic reduction of van der Waals forces between particles to avoid coagulation between particles. Moreover, the $FeSe_2$ HPs[47] are the most promising HPs among others owing to the semiconductor nature of $FeSe_2$ and their good structural integrity. Therefore, I selected $FeSe_2$ HPs as the active species to be investigated in the following chapters.

1.6.2 Chapter 2 The Selection of Electrolyte Systems for Hedgehog Particles

This chapter will include the complete procedure in selecting a suitable electrolyte system for $FeSe_2$ HPs. The key factors that will be considered are the solvent and the supporting electrolyte of the electrolyte system, and the working electrode. The candidates in each categories are listed below.

Solvent: acetonitrile and *N,N*-dimethylformamide (DMF).

Supporting electrolyte: lithium trifluoromethanesulfonate (LiTf), tetrabutylammonium hexafluorophosphate ($TBAPF_6$), and tetrabutylammonium Perchlorate (TBAP or $TBAClO_4$).

Working electrode: glassy carbon and gold disk.

By comparing the CVs of different electrolyte systems, the most competitive electrolyte system of $FeSe_2$ HPs will be chosen based on the best electrochemical activities.

1.6.3 Chapter 3 The Electrochemical Activities of Iron Diselenide Hedgehog Particles

In this chapter, I discuss how to assess the electrochemical activities of $FeSe_2$ HPs in the selected electrolyte system by many aspects consisting of dispersibility, resistance, adsorption, redox processes, electrochemical and structural stability.

Dispersibility: observed the aggregation from the dispersion over a long period of time.

Resistance: performed Electrochemical Impedance Spectroscopy (EIS) tests to calculate the uncompensated resistance (R_u).

Adsorption: conducted CV experiments with different scan rates to find the relationship between the peak current versus the square root of scan rate ($\sqrt{v}$).

Redox processes: executed CV tests and followed the curve to draw conclusions regarding the reactions. Moreover, I also did CV experiments with different potential span to understand the electrochemistry.

Electrochemical and structural stability: performed long-term CV tests for 250 cycles (a total of 4 hours) and took SEM images before and after the experiments. Applied software to count the diameter of HPs and the length of the nanospikes and made the comparison between HPs as prepared and HPs after the long-term CV test.

From experimental results above, the electrolyte system of $FeSe_2$ HPs was electrochemically stable for a long period of time.

1.6.4 Chapter 4 The Charging Capacity of Iron Diselenide in the Electrolyte System

This chapter describes a couple of ways to calculate the charging capacity of $FeSe_2$ HPs in this electrolyte system. One of the methods is to perform bulk electrolysis experiments. On the basis of the bulk electrolysis plot along with calculation using the particle concentration from the nanoparticle tracking analysis (NTA) experiments, I was able to calculate the charging capacity of $FeSe_2$ HPs based on a single HP or a $FeSe_2$ crystalline unit cell.

Our collaborator Dr. Bingcheng Luo performed simulations using Density Functional Perturbation Theory (DFPT) and calculated the phonon dispersion of $FeSe_2$ with different charges. The computational results matched well with the experimental results. By comparing the charging capacity of $FeSe_2$ HPs with previously studied colloidal semiconductor QDs[1,8], HPs surpassed them in the aspect of per crystalline unit cell, per surface area of a single particle and per volume of a single particle. I also compare the charges per surface area on the working electrode with these electrolyte systems and other electrode systems as well.

The structural integrity was examined similarly by comparing the SEM images, average diameter of HPs and average length of nanospikes.

1.6.5 Chapter 5 Conclusions and Future Work

This chapter starts with the conclusion of this dissertation, summarizing the electrochemical properties of $FeSe_2$ HPs in DMF. Next, I envision the future work that can be

done, mostly in the electrocatalysis field. I discuss the novelty of the idea for $FeSe_2$ HPs to act like homogeneous electrocatalysts in heterogeneous electrocatalytic systems and potential reactions that are worth working on as a starting point. Finally, the originality, contribution and significance of this future work is conveyed, highlighting the importance of my dissertation.

1.7 References

(1) Haram, S. K.; Quinn, B. M.; Bard, A. J. Electrochemistry of CdS Nanoparticles: A Correlation between Optical and Electrochemical Band Gaps. *Journal of the American Chemical Society*. American Chemical Society 2001, pp 8860–8861. https://doi.org/10.1021/ja0158206.

(2) Bae, Y.; Myung, N.; Bard, A. J. Electrochemistry and Electrogenerated Chemiluminescence of CdTe Nanoparticles. *Nano Lett.* **2004**, *4* (6), 1153–1161. https://doi.org/10.1021/nl049516x.

(3) Haram, S. K.; Kshirsagar, A.; Gujarathi, Y. D.; Ingole, P. P.; Nene, O. A.; Markad, G. B.; Nanavati, S. P. Quantum Confinement in CdTe Quantum Dots: Investigation through Cyclic Voltammetry Supported by Density Functional Theory (DFT). *J. Phys. Chem. C* **2011**, *115* (14), 6243–6249. https://doi.org/10.1021/jp111463f.

(4) Markad, G. B.; Battu, S.; Kapoor, S.; Haram, S. K. Interaction between Quantum Dots of CdTe and Reduced Graphene Oxide: Investigation through Cyclic Voltammetry and Spectroscopy. *J. Phys. Chem. C* **2013**, *117* (40), 20944–20950. https://doi.org/10.1021/jp406679s.

(5) Inamdar, S. N.; Ingole, P. P.; Haram, S. K. Determination of Band Structure Parameters and the Quasi-Particle Gap of CdSe Quantum Dots by Cyclic Voltammetry. *ChemPhysChem* **2008**, *9* (17), 2574–2579. https://doi.org/10.1002/cphc.200800482.

(6) Maiti, S.; Dana, J.; Jadhav, Y.; Debnath, T.; Haram, S. K.; Ghosh, H. N. Electrochemical Evaluation of Dopant Energetics and the Modulation of Ultrafast Carrier Dynamics in Cu-Doped CdSe Nanocrystals. *J. Phys. Chem. C* **2017**, *121* (48), 27233–27240. https://doi.org/10.1021/acs.jpcc.7b10262.

(7) Kucur, E.; Riegler, J.; Urban, G. A.; Nann, T. Determination of Quantum Confinement in CdSe Nanocrystals by Cyclic Voltammetry. *J. Chem. Phys.* **2003**, *119* (4), 2333–2337. https://doi.org/10.1063/1.1582834.

(8) Albery, W. J.; Bartlett, P. N.; Porter, J. D. The Electrochemistry of Colloidal Semiconductor Particles: Experiments on CdS and TiO2. *J. Electrochem. Soc.* **1984**, *131* (12), 2896–2900. https://doi.org/10.1149/1.2115438.

(9) Mulvaney, P.; Giersig, M.; Henglein, A. Surface Chemistry of Colloidal Gold: Deposition of Lead and Accompanying Optical Effects. *J. Phys. Chem.* **1992**, *96* (25), 10419–10424. https://doi.org/10.1021/j100204a056.

(10) Scholz, F.; Schröder, U.; Gulaboski, R. *Electrochemistry of Immobilized Particles and Droplets*, 2nd ed.; Springer, 2015. https://doi.org/10.1007/b137048.

(11) Campbell, F. W.; Compton, R. G. The Use of Nanoparticles in Electroanalysis: An Updated Review. *Anal. Bioanal. Chem.* **2010**, *396* (1), 241–259.

https://doi.org/10.1007/s00216-009-3063-7.

(12) de la Cueva, L.; Lauwaet, K.; Otero, R.; Gallego, M.; Juarez, B. H. Effect of Chloride Ligands on CdSe Nanocrystals by Cyclic Voltammetry and X-Ray Photoelectron Spectroscopy. *J. Phys. Chem. C* **2014**, *118*. https://doi.org/10.1021/jp4118425.

(13) Myung, N.; Ding, Z.; Bard, A. J. Electrogenerated Chemiluminescence of CdSe Nanocrystals. *Nano Lett.* **2002**, *2* (11), 1315–1319. https://doi.org/10.1021/nl0257824.

(14) Myung, N.; Bae, Y.; Bard, A. J. Effect of Surface Passivation on the Electrogenerated Chemiluminescence of CdSe/ZnSe Nanocrystals. *NANO Lett.* **2003**, *3* (8), 1053–1055. https://doi.org/10.1021/nl034354a.

(15) Conway, B. E.; Bockris, J. O.; White, R. E. *Modern Aspects of Electrochemistry No.28*, 1st ed.; Springer: New York, 1996.

(16) Cao, Q.; Hensley, D. K.; Lavrik, N. V.; Venton, B. J. Carbon Nanospikes Have Better Electrochemical Properties than Carbon Nanotubes Due to Greater Surface Roughness and Defect Sites. *Carbon N. Y.* **2019**, *155*, 250–257. https://doi.org/10.1016/j.carbon.2019.08.064.

(17) Khairy, M.; El-Safty, S. A. Mesoporous NiO Nanoarchitectures for Electrochemical Energy Storage: Influence of Size, Porosity, and Morphology. *RSC Adv.* **2013**, *3* (45), 23801–23809. https://doi.org/10.1039/c3ra44465a.

(18) Sankar, K. V.; Seo, Y.; Lee, S. C.; Liu, S.; Kundu, A.; Ray, C.; Jun, S. C. Cobalt Carbonate Hydroxides as Advanced Battery-Type Materials for Supercapatteries: Influence of Morphology on Performance. *Electrochim. Acta* **2018**, *259*, 1037–1044. https://doi.org/10.1016/j.electacta.2017.11.009.

(19) Becking, J.; Gröbmeyer, A.; Kolek, M.; Rodehorst, U.; Schulze, S.; Winter, M.; Bieker, P.; Stan, M. C. Lithium-Metal Foil Surface Modification: An Effective Method to Improve the Cycling Performance of Lithium-Metal Batteries. *Adv. Mater. Interfaces* **2017**, *4* (16). https://doi.org/10.1002/admi.201700166.

(20) Wang, K.; Pei, P.; Ma, Z.; Xu, H.; Li, P.; Wang, X. Morphology Control of Zinc Regeneration for Zinc-Air Fuel Cell and Battery. *J. Power Sources* **2014**, *271*, 65–75. https://doi.org/10.1016/j.jpowsour.2014.07.182.

(21) Chen, J. C. M.; Yang, J.; Cheng, M. M. C. Induced Nanoscale Roughness of Current Collectors Enhances Lithium Ion Battery Performances. *J. Power Sources* **2019**, *430*, 169–174. https://doi.org/10.1016/j.jpowsour.2019.05.026.

(22) Qu, F.; Li, C.; Wang, Z.; Strunk, H. P.; Maier, J. Metal-Induced Crystallization of Highly Corrugated Silicon Thick Films as Potential Anodes for Li-Ion Batteries. *ACS Appl. Mater. Interfaces* **2014**, *6* (11), 8782–8788. https://doi.org/10.1021/am501570w.

(23) Wang, M.; Emre, A.; Tung, S.; Gerber, A.; Wang, D.; Huang, Y.; Cecen, V.; Kotov, N. A.

Biomimetic Solid-State Zn2+ Electrolyte for Corrugated Structural Batteries. *ACS Nano* **2019**, *13* (2), 1107–1115. https://doi.org/10.1021/acsnano.8b05068.

(24) da Silva, A. H. M.; Raaijaman, S. J.; Santana, C. S.; Assaf, J. M.; Gomes, J. F.; Koper, M. T. M. Electrocatalytic CO2 Reduction to C2+ Products on Cu and CuxZny Electrodes: Effects of Chemical Composition and Surface Morphology. *J. Electroanal. Chem.* **2020**, *880*, 114750. https://doi.org/10.1016/j.jelechem.2020.114750.

(25) Roberts, F. S.; Kuhl, K. P.; Nilsson, A. Electroreduction of Carbon Monoxide Over a Copper Nanocube Catalyst: Surface Structure and PH Dependence on Selectivity. *ChemCatChem* **2016**, *8* (6), 1119–1124. https://doi.org/10.1002/cctc.201501189.

(26) Kibria, M. G.; Dinh, C.-T.; Seifitokaldani, A.; De Luna, P.; Burdyny, T.; Quintero-Bermudez, R.; Ross, M. B.; Bushuyev, O. S.; García de Arquer, F. P.; Yang, P.; Sinton, D.; Sargent, E. H. A Surface Reconstruction Route to High Productivity and Selectivity in CO_2 Electroreduction toward C_{2+} Hydrocarbons. *Adv. Mater.* **2018**, *30* (49), 1804867. https://doi.org/10.1002/adma.201804867.

(27) Chen, Z.; Higgins, D.; Chen, Z. Electrocatalytic Activity of Nitrogen Doped Carbon Nanotubes with Different Morphologies for Oxygen Reduction Reaction. *Electrochim. Acta* **2010**, *55* (16), 4799–4804. https://doi.org/10.1016/j.electacta.2010.03.057.

(28) Jiang, K.; Huang, Y.; Zeng, G.; Toma, F. M.; Goddard, W. A.; Bell, A. T. Effects of Surface Roughness on the Electrochemical Reduction of CO2 over Cu. *ACS Energy Lett.* **2020**, *5* (4), 1206–1214. https://doi.org/10.1021/acsenergylett.0c00482.

(29) Gorchakov, E. V.; Perevezentseva, D. O.; Fedota, N. V.; Belyaev, V. A.; Bagamaev, B. M. Determination of Cystein in Biology Solids by Electrochemical Methods with Gold Colloidal Particles. *World Appl. Sci. J.* **2014**, *29* (12), 1591–1594. https://doi.org/10.5829/idosi.wasj.2014.29.12.13989.

(30) Brown, K. R.; Fox, A. P.; Natan, M. J. Morphology-Dependent Electrochemistry of Cytochrome c at Au Colloid-Modified SnO2 Electrodes. *J. Am. Chem. Soc.* **1996**, *118* (5), 1154–1157. https://doi.org/10.1021/ja952951w.

(31) Armstrong, F. A.; Hill, H. A. O.; Oliver, B. N.; Psalti, I. S. M.; Bond, A. M. Electrochemistry of Cytochrome c, Plastocyanin, and Ferredoxin at Edge- and Basal-Plane Graphite Electrodes Interpreted via a Model Based on Electron Transfer at Electroactive Sites of Microscopic Dimensions in Size. *J. Am. Chem. Soc.* **1989**, *111* (26), 9185–9189. https://doi.org/10.1021/ja00208a008.

(32) Allen, P. M.; Allen, H.; Hill, O.; Walton, N. J. Surface Modifiers for the Promotion of Direct Electrochemistry of Cytochrome C. *J. Electroanal. Chem.* **1984**, *178* (1), 69–86. https://doi.org/10.1016/S0022-0728(84)80024-8.

(33) Asefa, T.; Shi, Y. L. Corrugated and Nanoporous Silica Microspheres: Synthesis by Controlled Etching, and Improving Their Chemical Adsorption and Application in Biosensing. *J. Mater. Chem.* **2008**, *18* (46), 5604–5614. https://doi.org/10.1039/b811034d.

(34) De Levie, R. The Influence of Surface Roughness of Solid Electrodes on Electrochemical Measurements. *Electrochim. Acta* **1965**, *10* (2), 113–130. https://doi.org/10.1016/0013-4686(65)87012-8.

(35) Clausmeyer, J.; Masa, J.; Ventosa, E.; Öhl, D.; Schuhmann, W. Nanoelectrodes Reveal the Electrochemistry of Single Nickel Hydroxide Nanoparticles. *Chem. Commun.* **2016**, *52* (11), 2408–2411. https://doi.org/10.1039/c5cc08796a.

(36) Cheng, W.; Compton, R. G. Electrochemical Detection of Nanoparticles by 'Nano-Impact' Methods. *TrAC Trends Anal. Chem.* **2014**, *58*, 79–89. https://doi.org/https://doi.org/10.1016/j.trac.2014.01.008.

(37) Henstridge, M. C.; Ward, K. R.; Compton, R. G. The Marcus-Hush Model of Electrode Kinetics at a Single Nanoparticle. *J. Electroanal. Chem.* **2014**, *712*, 14–18. https://doi.org/https://doi.org/10.1016/j.jelechem.2013.10.012.

(38) Birla Singh, M.; Kant, R. Theory of Anomalous Dynamics of Electric Double Layer at Heterogeneous and Rough Electrodes. *J. Phys. Chem. C* **2014**, *118* (10), 5122–5133. https://doi.org/10.1021/jp410999b.

(39) Tschulik, K.; Batchelor-McAuley, C.; Toh, H.-S.; Stuart, E. J. E.; Compton, R. G. Electrochemical Studies of Silver Nanoparticles: A Guide for Experimentalists and a Perspective. *Phys. Chem. Chem. Phys.* **2014**, *16* (2), 616–623. https://doi.org/10.1039/C3CP54221A.

(40) Burton, E. F.; Bishop, E. Coagulation of Colloidal Solutions by Electrolytes: Influence of Concentration of Sol. *J. Phys. Chem.* **1920**, *24* (9), 701–715. https://doi.org/10.1021/j150207a002.

(41) Desai, B. N.; Barve, P. M. Coagulation of Colloids by Electrolytes. *Nature*. 1931, pp 907–908. https://doi.org/10.1038/128907c0.

(42) Bahng, J. H.; Yeom, B.; Wang, Y.; Tung, S. O.; Hoff, J. D.; Kotov, N. Anomalous Dispersions of "hedgehog" Particles. *Nature* **2015**, *517* (7536), 596–599. https://doi.org/10.1038/nature14092.

(43) Montjoy, D. G.; Bahng, J. H.; Eskafi, A.; Hou, H.; Kotov, N. A. Omnidispersible Hedgehog Particles with Multilayer Coatings for Multiplexed Biosensing. *J. Am. Chem. Soc.* **2018**, *140* (25), 7835–7845. https://doi.org/10.1021/jacs.8b02666.

(44) Montjoy, D. G.; Hou, H.; Bahng, J. H.; Kotov, N. A. Omnidispersible Microscale Colloids with Nanoscale Polymeric Spikes. *Chem. Mater.* **2020**, *32* (23), 9897–9905. https://doi.org/10.1021/acs.chemmater.0c02472.

(45) Montjoy, D. G.; Hou, H.; Bahng, J. H.; Eskafi, A.; Jiang, R.; Kotov, N. A. Photocatalytic Hedgehog Particles for High Ionic Strength Environments. *ACS Nano* **2021**, *15* (3), 4226–4234. https://doi.org/10.1021/acsnano.0c05992.

(46) Zakzeski, J.; Bruijnincx, P. C. A.; Jongerius, A. L.; Weckhuysen, B. M. The Catalytic Valorization of Lignin for the Production of Renewable Chemicals. *Chem. Rev.* **2010**, *110* (6), 3552–3599. https://doi.org/10.1021/cr900354u.

(47) Deng, D.; Hao, C.; Sen, S.; Xu, C.; Král, P.; Kotov, N. A. Template-Free Hierarchical Self-Assembly of Iron Diselenide Nanoparticles into Mesoscale Hedgehogs. *J. Am. Chem. Soc.* **2017**, *139* (46), 16630–16639. https://doi.org/10.1021/jacs.7b07838.

(48) Srikant, V.; Clarke, D. R. On the Optical Band Gap of Zinc Oxide. *J. Appl. Phys.* **1998**, *83* (10), 5447. https://doi.org/10.1063/1.367375.

Chapter 2 The Selection of Electrolyte Systems for Hedgehog Particles

2.1 Background and Approach

The electrolyte systems are comprised of three components, including active species, solvent, and the supporting electrolyte. The active species is the material that is expected to demonstrate electrochemical activities (oxidation, reduction, adsorption, desorption, *etc.*) in the potential range. We should expect to see peaks in the CV curves related to these electrochemical activities that are characteristic of the active species.

The solvent is the substance in which the active species and supporting electrolyte dissolve or disperse in to produce a solution or dispersion. Active species and supporting electrolyte are expected to have a good solubility or dispersibility in the picked solvent because active materials and ions in the supporting electrolyte need to move between electrodes in order to maintain charge neutrality throughout different electrochemical courses. Generally speaking, solvents can be divided into two categories, aqueous and non-aqueous. Water is the only aqueous solvent. There are several requirements for a good non-aqueous solvent. Firstly, it needs to be electrochemically stable for a large potential range. Secondly, a high polarity is ideal because the electrolyte systems should be conductive. Thirdly, a low viscosity is necessary in order to avoid mass transport issues especially when the concentration of active species and supporting electrolyte is increased.

The supporting electrolyte (or supporting salt) is usually a salt that is highly dissolvable in the selected solvent to increase the conductivity of the system. Empirically, a maximum solubility above 1 mol/L will be ideal. Meanwhile, the supporting electrolyte should be electrochemically

stable within a wide potential range, i.e. no electrochemical activities, in order not to interfere with the judgement of electrochemical properties of active species.

CV is the primary tool to select the electrolyte system for $FeSe_2$ HPs. Firstly, a CV from the blank system will be conducted. The blank system is consisted of both solvent and supporting electrolyte. We anticipate a flat CV curve for a wider potential range without any minor peaks. In this circumstance, without adding the active species, one should expect all peaks related to supporting electrolyte. (By conducting some necessary preliminary CV experiments, one should eliminate the possibility that the solvent and the electrode itself will react in the potential range before moving to the CV of blank systems.) Then, the best supporting electrolyte will be applied to the electrolyte system adding a sufficient amount of $FeSe_2$ HPs. We hope to see some peaks within the potential range. Since we have already confirmed that the supporting electrolyte generate no peaks in the range, all the peaks seen can be ascribed to $FeSe_2$ HPs. We also would like to see a larger current response because this represents a higher activities of the electrolyte system.

In the electrolyte system of $FeSe_2$ HPs, we are looking at the electrochemical performance of HPs, therefore, $FeSe_2$ HP is the active species in this scenario. As for the solvent and supporting electrolyte candidates, we referred studies related to the electrochemical properties of electrolyte systems of semiconductor NPs in the past. See Table 2-1 below.

Table 2-1 Experimental setups for studies regarding electrochemical properties of semiconductor NPs in different electrolytes.

Title	Working Electrode	Counter Electrode	Reference Electrode	Nanoparticle Concentration	Salt Concentration	Solvent	Glove Box
Electrogenerated Chemiluminescence of CdSe Nanocrystals[1]	Pt disk	Pt wire	Ag wire quasi	50-60 mg	0.1 M TBAP	2 mL CH_2Cl_2	Yes
Electrochemistry and Electrogenerated Chemiluminescence of CdTe Nanoparticles[2]	Pt disk	Pt wire	Ag wire quasi	-	TBAP or $TBAPF_6$	CH_2Cl_2 or 5:1 C_6H_6:CH_3CN	Yes
Effect of Chloride Ligands on CdSe Nanocrystals by Cyclic Voltammetry and X-ray Photoelectron Spectroscopy[3]	Glassy Carbon	Pt sheet	Ag/Ag^+ in acetonitrile	10 μL drop cast on GCWE	0.1 M TBAP	acetonitrile	Yes
Interaction between Quantum Dots of CdTe and Reduced Graphene Oxide: Investigation through Cyclic Voltammetry and Spectroscopy[4]	Au disk	Pt wire loop	Hg/HgO in sat. $Ca(OH)_2$	1 mg/mL	buffer of pH 9.2 (0.1 M Na_2SO_4 and 0.02 M $Na_2B_4O_7$)		No
Quantum Confinement in CdTe Quantum Dots: Investigation through Cyclic Voltammetry Supported by Density Functional Theory (DFT)[5]	Pt disk	Pt wire loop	Ag wire quasi (Fc/Fc^+)	-	0.1 M TBAP	CH_2Cl_2	Yes
Determination of Band Structure Parameters and the Quasi-Particle Gap of CdSe Quantum Dots by Cyclic Voltammetry[6]	Glassy Carbon	Pt wire loop	Ag wire quasi (Fc/Fc^+)	1 mg/mL	0.1 M TBAP	DMSO:C_7H_8 4:1	Yes
Electrochemical Evaluation of Dopant Energetics and the Modulation of Ultrafast Carrier Dynamics in Cu-Doped CdSe Nanocrystals[7]	Au disk	Pt wire loop	Ag wire quasi (Fc/Fc^+)	1 mg/mL	0.1 M TBAP	CH_2Cl_2	Yes
Electrochemistry of CdS Nanoparticles: A Correlation between Optical and Electrochemical Band Gaps[8]	Pt and Au	Pt coil	Ag wire quasi (Fc/Fc^+)	1 mg/mL	0.1 M THAP	DMF	Yes

From the table, we can see that two supporting salts are frequently used - $TBAPF_6$ (tetrabutylammonium hexafluorophosphate) and TBAP (tetrabutylammonium perchlorate). I also would like to add LiTf in the candidate list. LiTf is the supporting electrolyte that I chose and frequently applied in my previous project[9]. LiTf can greatly facilitate the conductivity increase and is electrochemically stable at a wide potential window.

As for the solvent selection, acetonitrile and DMF stood out due to their specific physical properties. Both solvents are broadly applied as solvents in various electrolyte systems because they have high polarity and low viscosity. Although HPs can maintain a great dispersibility in water, the potential window of water is sacrificed by water electrolysis at 1.23 V. We may not be able to see the full electrochemical activities of HPs if the value of peak separation is larger than the value of band gap for $FeSe_2$ HPs. So, water was not considered as a solvent in the electrolyte system of HPs.

Apart from the three components in the electrolyte system, the material of the working electrode is crucial as well since the electrochemical activities are recorded on the surface of the working electrode. Generally, the material of working electrode can be categorized as metal or non-metal. For non-metal working electrodes, glassy carbon is the most popular due to carbon's high conductivity and poor activity to various types of catalytic reactions such as Hydrogen Evolution Reaction (HER), Oxygen Evolution Reaction (OER), CO_2 reduction, *etc*. For metal working electrodes, there are quite a few options. Platinum has a great activities over many reactions but platinum is also electrocatalytically active which may bring problems in differentiating from the electrochemical activities related to HPs. Although all of the electrochemical tests were performed inside a glove box, it will be better to avoid any issue related

to electrocatalysis. Thus, gold electrodes can be a great option as a metal working electrode. Below is a full list of candidates in all divisions in the electrolyte system of $FeSe_2$ HPs.

Table 2-2 A Full list of candidates in all groups in the electrolyte system of $FeSe_2$ HPs.

Active Species	Solvent	Supporting Electrolyte	Working Electrode
	DMF	LiTf	Glassy Carbon
$FeSe_2$ HPs	Acetonitilre	TBAP	Gold (Disk)
		$TBAPF_6$	

2.2 Experimental

2.2.1 Chemicals

N,N-dimethylformamide (ACS reagent, ≥ 99.8%), acetonitrile (anhydrous, 99.8%), lithium trifluoromethanesulfonate (LiTf, 99.95%, trace metals basis), tetrabutylammonium hexafluorophosphate (TBAP, 98%) were purchased from Sigma-Aldrich. Tetrabutylammonium perchlorate (98.0+%) was purchased from TCI America™. No further purification needed for materials received.

2.2.2 Synthesis of $FeSe_2$ HPs

Iron (III) chloride (reagent grade, 97%), oleic acid (technical grade, 90%), 1-octadecene (technical grade, 90%), N,N-dimethylformamide (ACS reagent, ≥99.8%), oleylamine (technical grade, 70%) and chloroform (HPLC plus, ≥99.9%) were purchased from Sigma-Aldrich. 1-Dodecanethiol (≥98%) was purchased from Aldrich. Selenium powder (200 mesh, 99.999%

(metal basis), Alfa Aesar) was purchased from Fisher Scientific. No further purification needed for materials received.

In order to satisfy the requirement of electrochemical measurements, it is crucial to scale up the previous synthesis procedure.[10] The preliminary test results indicated that the self-assembly time is the most important parameter in controlling the structure of HPs during scale up. It was found that 120 min self-assembly time is necessary for all the HPs to grow to the size and structure similar to the previously synthesized HPs.

In a typical synthesis reaction, 0.8110 g iron (III) chloride, 1 mL oleic acid, 20 mL 1-dodecanethiol, 40 mL oleylamine, and 60 mL 1-octadecene were added in a 250 mL 3-neck flask in argon atmosphere. The mixture was stirred slowly, and the temperature of the solution increased from room temperature to 175 ℃ over 30 min. During the process, Fe^{3+} was reduced to Fe^{2+}, and the color of the mixture changed from dark to clear brown with increasing temperature, assuring the reduction of Fe^{3+}. At the same time, 0.7900 g selenium powder was mixed well with 14 mL oleylamine and 6 mL 1-dodecanethiol. When the temperature of solution in 3-neck flask reached 175 ℃, the selenium solution was added immediately into the 3-neck flask. The color of the solution turned black instantaneously, indicating the formation of iron selenide nanoparticles. The mixture was stirred slowly for 120 min for iron selenide to grow into HPs. After the synthesis, the 3-neck flask was cooled down to room temperature rapidly using an ice bath. The suspension was washed three times by centrifugation using chloroform as the washing agent. Then, the black suspensions were exchanged for three times by ethanol to remove chloroform. Next, the dispersions were exchanged for at least three times by water to remove ethanol. The final suspensions in water were frozen in the freezer before drying under vacuum for 48 hours. The black precipitates were harvested and stored inside the glove box for future use.

2.2.3 Cyclic Voltammetry

CV test is the most essential tool to investigate the electrochemical properties of active species. We apply a three-electrode setup for CV tests. The three electrodes include working electrode, reference electrode, and counter electrode. The current is measured between the working electrode and the counter electrode, and the voltage is measured between the working electrode and the reference electrode. In a CV experiment, the potential is ramped linearly versus time starting from the initial potential. When the potential reaches its set potential, it will ramp in the other direction back to its original potential. This can be cycled as many time as needed.

In the electrolyte system, either gold disk (3 mm, MF-2114, BASi) or glassy carbon electrode (3 mm, MF-2012, BASi) were used as the working electrode. The counter electrode was a platinum coil auxiliary electrode (MW-1033, BASi). The reference electrode was Ag/Ag^+ (MF-2062, BASi). This three-electrode CV cell is produced by Glass Shop in the Department of Chemistry in University of Michigan – Ann Arbor.

CV tests were carried out by Autolab PGSTAT302N combined with the software named NOVA (Metrohm Autolab) to set up different procedures, record data and initially analyze the data.

2.3 Results and Discussion

2.3.1 The Electrolyte System of $FeSe_2$ HPs in DMF (Glassy Carbon Working Electrode)

In the blank system in DMF using glassy carbon working electrode, and based on Table 2-3 and Figure 2-1, LiTf had the largest potential range of 3.5 V. A similar redox couple can be

witnessed at the potential below 1.0 V vs. Ag/Ag^+ for TBAP and $TBAPF_6$. Due to the similarity of the peak shape and intensity, it is reasonable to anticipate that this redox couple is related to TBA salt. Thus, the potential window of both TBA salts would be limited to potential above -1.0 V, and LiTf should be applied in the electrolyte system adding $FeSe_2$ HPs.

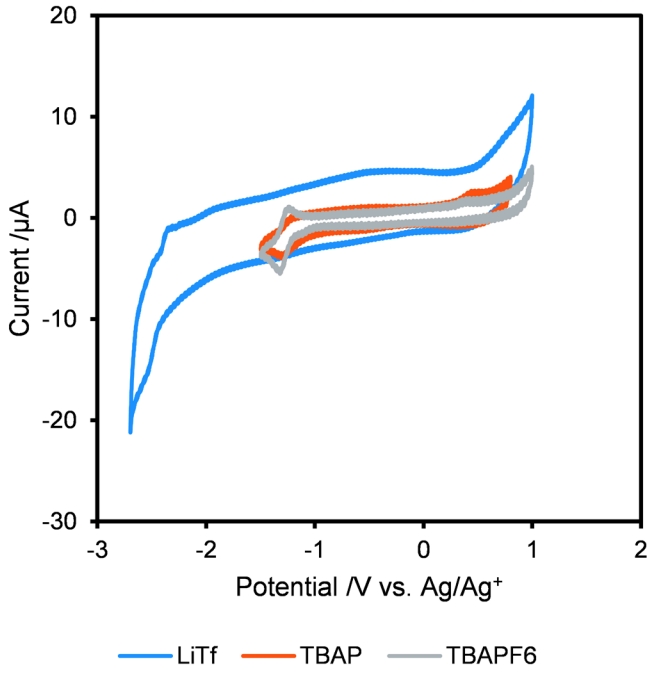

Figure 2-1 CVs of 0.1 M supporting electrolyte (LiTf in blue, TBAP in orange, $TBAPF_6$ in gray) in DMF. Scan rate of 0.1 V/s, the 5th cycle, working electrode of glassy carbon.

Table 2-3 Potential window of supporting electrolytes in DMF (glassy carbon working electrode).

Supporting Electrolyte	Potential Window	Supporting Electrolyte	Potential Window	Supporting Electrolyte	Potential Window
LiTf	-2.5 V – 1.0 V	TBAP	-1.2 V – 0.8 V	$TBAPF_6$	-1.2 V – 1.0 V

Adding 2 mg/mL $FeSe_2$ HPs to the blank system, CVs were expected to show the electrochemical properties of HPs because supporting electrolytes were examined to have no electrochemical activities in the CVs of blank systems. From Figure 2-2, there is an oxidation peak at 0.7 V vs. Ag/Ag^+ and a reduction peak at -1.0 V vs. Ag/Ag^+ that can be attributed to

electrochemical activities of $FeSe_2$ HPs. Therefore, the peak separation is 1.7 V. Considering the band gap for $FeSe_2$, the value of peak separation is larger than the value of the band gap.

The dispersion of 2 mg/mL $FeSe_2$ HPs in DMF is dense, but the current response is less than 10 μA, which is small considering the amount of HPs in the dispersion. Although the conductivity of glassy carbon is great among other non-metal electrodes, it still cannot be able to compare with some metal electrode including gold electrode. The choice of working electrode materials will affect the rate of electron transfer. As a result, it would be more beneficial if we switch to a gold disk working electrode to see if it can get better electrochemical activities for $FeSe_2$ HPs.

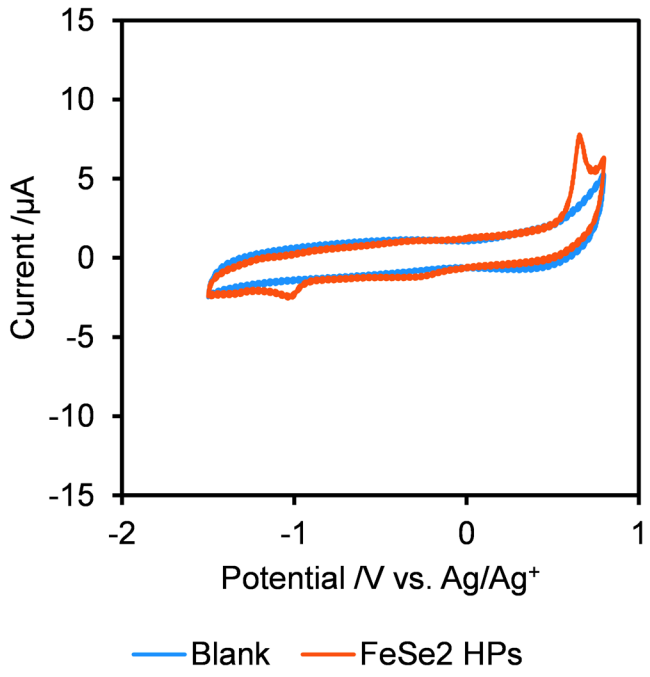

Figure 2-2 CVs of 2 mg/mL $FeSe_2$ HPs with 0.1 M LiTf in DMF (in orange). Blank CV of 0.1 M LiTf in DMF (in blue). Scan rate of 0.1 V/s, the 5th cycle, working electrode of glassy carbon.

2.3.2 The Electrolyte System of $FeSe_2$ HPs in DMF (Gold Disk Working Electrode)

Since TBA salts can react below -1.0 V vs. Ag/Ag^+ in DMF, TBAP was picked to compare with LiTf since $TBAPF_6$ should perform similarly to TBAP from the previous blank CVs. By switching to a gold disk working electrode, on the basis of Figure 2-3 and Table 2-4, both supporting electrolyte displayed a wide potential range of around 3.5 V. However, there were consistent minor peaks throughout the entire potential range for TBAP, which potentially can be an issue in differentiating the peaks regarding $FeSe_2$ HPs and those from TBAP. On the other hand, the CV curve of LiTf remains flat in the whole region. Therefore LiTf was chosen again to be utilized as the supporting electrolyte in the next step of adding $FeSe_2$ HPs to the system.

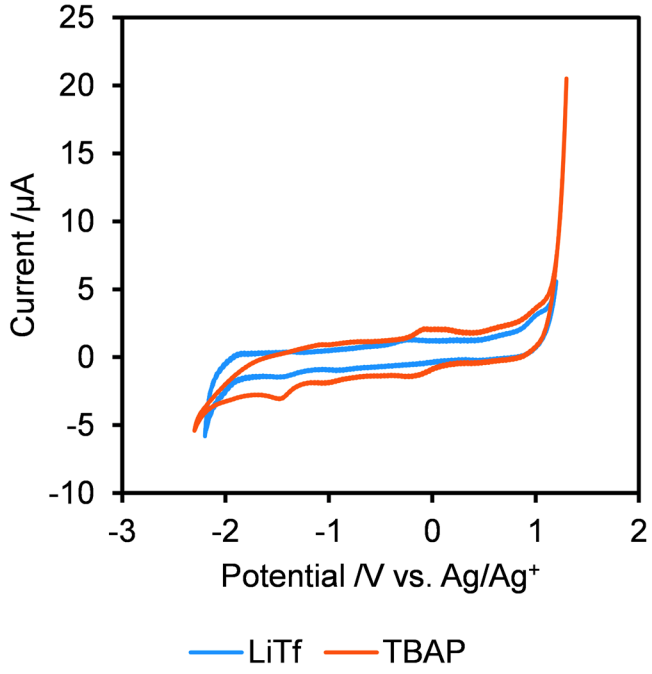

Figure 2-3 CVs of 0.1 M supporting electrolyte (LiTf in blue, TBAP in orange) in DMF. Scan rate of 0.1 V/s, the 5th cycle, working electrode of gold disk.

Table 2-4 Potential window of supporting electrolytes in DMF (gold disk working electrode).

Supporting Electrolyte	Potential Range	Supporting Electrolyte	Potential Range
LiTf	-2.2 V – 1.2 V	TBAP	-2.3 V – 1.3 V

By adding 2 mg/mL $FeSe_2$ HPs, the CV (Figure 2-4) looks completely different with a large peak intensity increase especially on the anodic side. The peak intensity of the oxidation peak located at 0.65 eV vs. Ag/Ag^+ significantly increases from less than 10 μA with the glassy carbon working electrode to more than 70 μA with the gold disk working electrode, approximately a tenfold increase in the current response. Some minor reduction peaks can be seen as well, with the biggest peak being at -0.2 V vs. Ag/Ag^+. Therefore, the peak separation can be 0.85 V. This may imply that the relationship between the value of peak separation and the value of optical band gap mentioned in Chapter 1 still stands for HPs.

As for the reason why $FeSe_2$ HPs displayed a better electrochemical activities by using gold disk, there are mainly two reasons. The rate of electron transfer can vary significantly from different materials. Here, gold has an advantage owing to the higher conductivity, and this will likely influence the kinetics of redox behaviors in the system. Moreover, glassy carbon has an amorphous structure, which may be a disadvantage for transporting HPs with a bulky and spiky morphology, compared to gold with an ordered structure.

Meanwhile, it would be valuable to see the different electrochemical activities in acetonitrile because its large potential range, high conductivity, and stability. The solvent effect may change the reaction rates, so all tests in both working electrodes were extended to systems in acetonitrile.

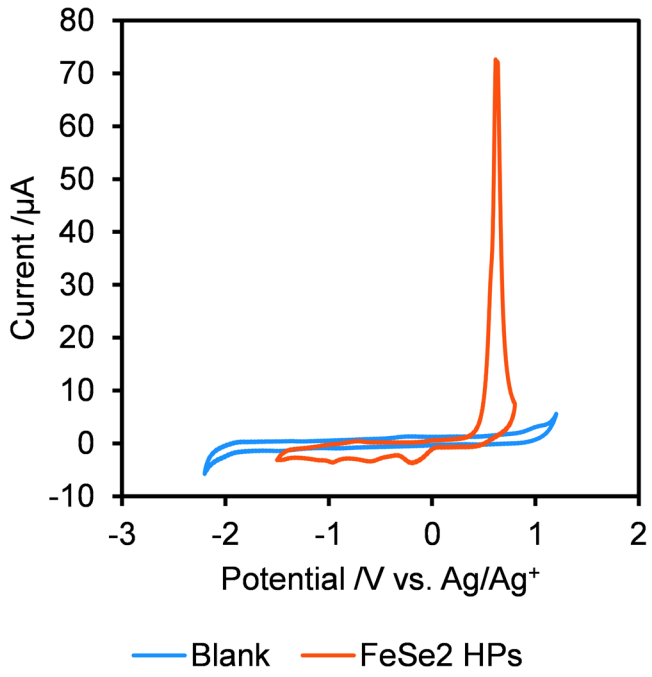

Figure 2-4 CVs of 2 mg/mL $FeSe_2$ HPs with 0.1 M LiTf in DMF (in orange). Blank CV of 0.1 M LiTf in DMF (in blue). Scan rate of 0.1 V/s, the 5th cycle, working electrode of gold disk.

2.3.3 The Electrolyte System of $FeSe_2$ HPs in Acetonitrile (Glassy Carbon Working Electrode)

Acetonitrile is very sensitive to water. Apart from opening and storing the chemicals inside the glove box, it is also important to store it in bottles with molecular sieves to absorb water. LiTf can absorb water easily, and it needs to be opened and stored inside the glove box for the whole time. Performing a CV using the glassy carbon working electrode on this system, there is a current increase in the cathodic scan (Figure 2-5) ascribed to the water reduction in the potential range. On the other hand, $TBAPF_6$ does not have any issues related to deliquescence and it has a wider potential window in the positive range (Figure 2-5, Table 2-5), which can be beneficial in electrolyte systems using acetonitrile as a solvent. Hence, $TBAPF_6$ will be used in the future electrochemical measurements.

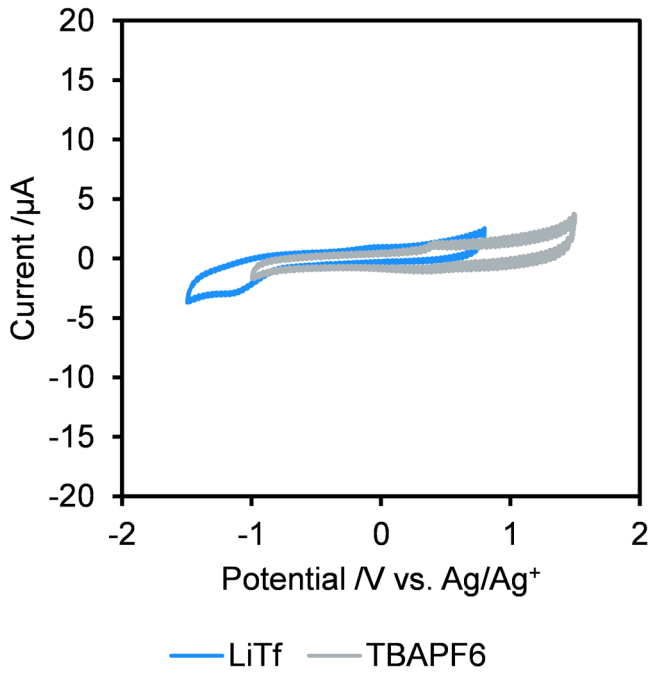

Figure 2-5 CVs of 0.1 M supporting electrolyte (LiTf in blue, $TBAPF_6$ in gray) in acetonitrile. Scan rate of 0.1 V/s, the 5th cycle, working electrode of glassy carbon.

Table 2-5 Potential window of supporting electrolytes in acetonitrile (glassy carbon working electrode).

Supporting Electrolyte	Potential Range	Supporting Electrolyte	Potential Range
LiTf	-1.5 V – 0.8 V	TBAP	-1.0 V – 1.5 V

When $FeSe_2$ HPs were added to the system, no obvious peaks can be seen over the potential range (Figure 2-6). There are a few possible reasons. First of all, empirically by switching the solvent from DMF to acetonitrile, it is anticipated that the peaks shift to the positive direction for about 0.2 – 0.3 V if the electrochemistry is the same in both solvents. However, it should be able to see these peaks considering the similar system in DMF (Figure 2-2). Secondly, it was unlikely due to the adsorption of acetonitrile on the surface of glassy carbon working electrode since this setup is commonly applied. Thirdly, the most possible reason can be due to the poor activity of $FeSe_2$ HPs. HPs can react under these circumstances, but either under very slow kinetics, or just a

small portions of HPs are able to react. $FeSe_2$ HPs may tend to be surrounded by acetonitrile, which makes it hard for the HPs to adsorb onto the surface of working electrode to react. Therefore, it is reasonable to look at the electrochemistry using the gold disk working electrode to see if the HPs perform differently.

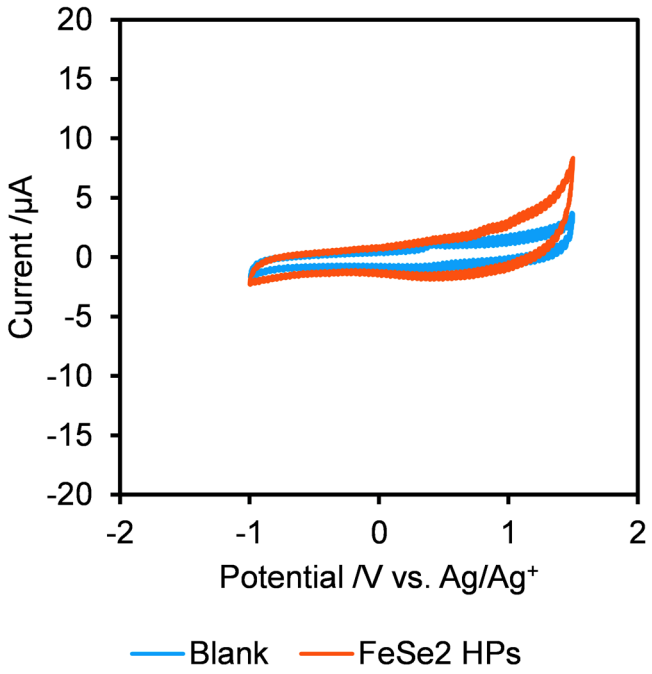

Figure 2-6 CVs of 2 mg/mL $FeSe_2$ HPs with 0.1 M LiTf in acetonitrile (in orange). Blank CV of 0.1 M LiTf in acetonitrile (in blue). Scan rate of 0.1 V/s, the 5th cycle, working electrode of glassy carbon.

2.3.4 The Electrolyte System of $FeSe_2$ HPs in Acetonitrile (Gold Disk Working Electrode)

Looking at the CVs of blank systems (Figure 2-7, Table 2-6) in acetonitrile using a gold disk working electrode, TBAP surpassed $TBAPF_6$ in the aspect of potential range. However, there is a minor oxidation peak at 0.5 V vs. Ag/Ag^+ that is worth noting in the CV of TBAP which may potentially disturb the appearance of electrochemical activities of $FeSe_2$ HPs in the further tests. Thus, $TBAP_6$ was utilized as the supporting electrolyte in CV experiments with HPs. Due to the deliquescence of LiTf, it was not considered among other supporting salts in this case.

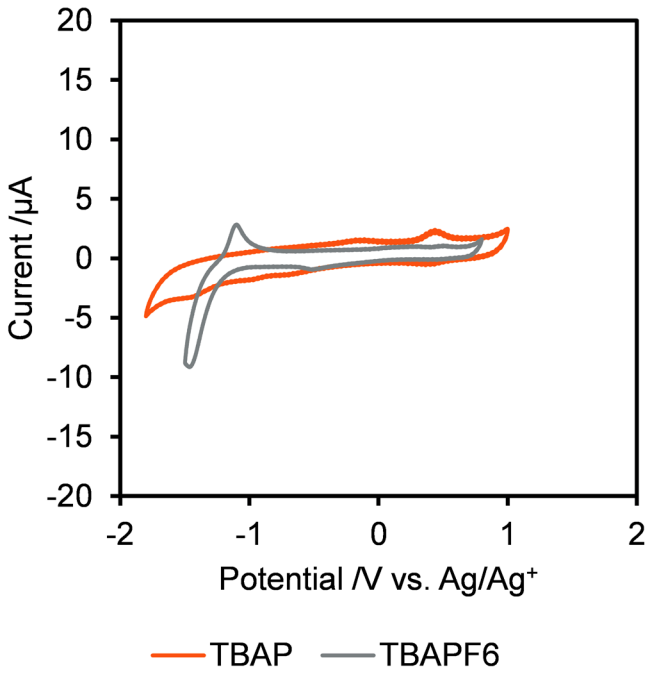

Figure 2-7 CVs of 0.1 M supporting electrolyte (TBAP in orange, $TBAPF_6$ in gray) in acetonitrile. Scan rate of 0.1 V/s, the 5th cycle, working electrode of gold disk.

Table 2-6 Potential window of supporting electrolytes in acetonitrile (gold disk working electrode).

Supporting Electrolyte	Potential Range	Supporting Electrolyte	Potential Range
TBAP	-1.8 V – 1.0 V	$TBAPF_6$	-1.2 V – 0.8 V

By adding 2 mg/mL FeSe2 HPs into the system with $TBAPF_6$, there are still no peaks throughout the potential range (Figure 2-8). This implies that the explanation of poor activities of $FeSe_2$ HPs still holds because these phenomena do not relate to the materials of the working electrode. In conclusion, acetonitrile is not a good solvent for electrolyte systems with $FeSe_2$ HPs. But it may work for other HPs due to the different functional group on the surface of the nanostructure.

In fact, the conductivity of the $FeSe_2$ dispersion is higher in DMF (11.1 mS/cm^2) compared to that in acetonitrile (9.3 mS/cm^2). Thus, the electrolyte system in DMF is more conductive than

the electrolyte system in acetonitrile, which will facilitate the transport of both HPs and corresponding ions in the suspension. Moreover, as mentioned in the previous studies on synthesizing $FeSe_2$ HPs and section 2.2.2, the ligands on the surface of the HPs include functional groups from 1-dodecanethiol, oleylamine and oleic acids. They are all polar solvents. At the same time, acetonitrile has a higher polarity than DMF. Therefore, it is possible that $FeSe_2$ HPs with these ligands are more likely to be trapped in cavities surrounded by acetonitrile molecules, which make them less able to be adsorbed on the surface of the working electrode. This solvent effect can seriously affect the reaction rates.

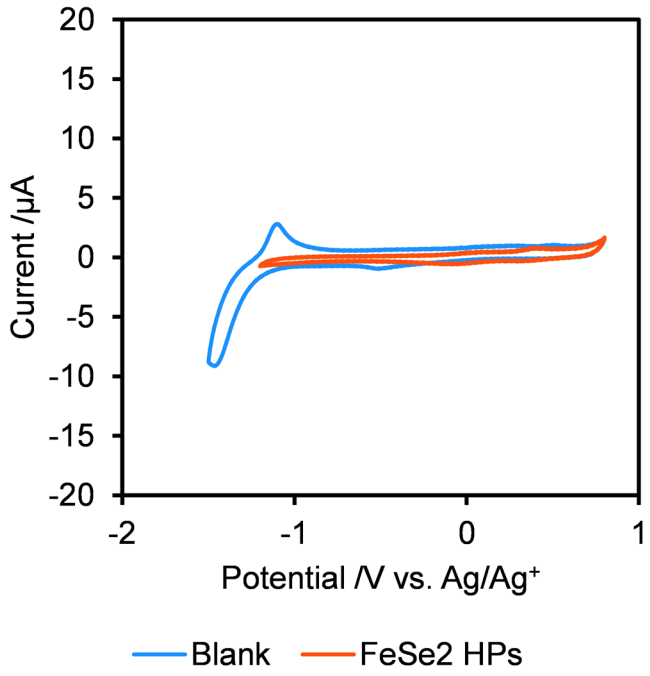

Figure 2-8 CVs of 2 mg/mL $FeSe_2$ HPs with 0.1 M LiTf in acetonitrile (in orange). Blank CV of 0.1 M LiTf in DMF (in blue). Scan rate of 0.1 V/s, the 5th cycle, working electrode of gold disk.

2.4 Conclusions

In respect to selecting the electrolyte for electrochemical studies of $FeSe_2$ HPs, these are the main conclusions. First of all, DMF was a better solvent than acetonitrile due to the better

activity of $FeSe_2$ HPs in DMF. The poor activities of $FeSe_2$ HPs in acetonitrile may be due to the solvent effect. Secondly, among all the supporting electrolyte candidates, LiTf stood out because of its wide potential range from -2.2 V to 1.2 V vs. Ag/Ag^+ (especially on the negative end) and minimal minor peaks across the potential window. The potential range of two other TBA salts, TBAP and $TBAPF_6$, was limited due to some minor reactions within the range. Thirdly, a gold disk working electrode is more favorable compared to a glassy carbon working electrode because of its excellent electrochemical activity related to $FeSe_2$ HPs. The glassy carbon working electrode is less conductive and it will possibly bring a slower slow electron transfer kinetics.

Hence, the electrolyte system of $FeSe_2$ HPs with 0.1 M LiTf in DMF using a gold disk working electrode is the most promising system and will be applied in all the future studies from here on out.

2.5 References

(1) Myung, N.; Ding, Z.; Bard, A. J. Electrogenerated Chemiluminescence of CdSe Nanocrystals. *Nano Lett.* **2002**, *2* (11), 1315–1319. https://doi.org/10.1021/nl0257824.

(2) Bae, Y.; Myung, N.; Bard, A. J. Electrochemistry and Electrogenerated Chemiluminescence of CdTe Nanoparticles. *Nano Lett.* **2004**, *4* (6), 1153–1161. https://doi.org/10.1021/nl049516x.

(3) de la Cueva, L.; Lauwaet, K.; Otero, R.; Gallego, M.; Juarez, B. H. Effect of Chloride Ligands on CdSe Nanocrystals by Cyclic Voltammetry and X-Ray Photoelectron Spectroscopy. *J. Phys. Chem. C* **2014**, *118*. https://doi.org/10.1021/jp4118425.

(4) Markad, G. B.; Battu, S.; Kapoor, S.; Haram, S. K. Interaction between Quantum Dots of CdTe and Reduced Graphene Oxide: Investigation through Cyclic Voltammetry and Spectroscopy. *J. Phys. Chem. C* **2013**, *117* (40), 20944–20950. https://doi.org/10.1021/jp406679s.

(5) Haram, S. K.; Kshirsagar, A.; Gujarathi, Y. D.; Ingole, P. P.; Nene, O. A.; Markad, G. B.; Nanavati, S. P. Quantum Confinement in CdTe Quantum Dots: Investigation through Cyclic Voltammetry Supported by Density Functional Theory (DFT). *J. Phys. Chem. C* **2011**, *115* (14), 6243–6249. https://doi.org/10.1021/jp111463f.

(6) Inamdar, S. N.; Ingole, P. P.; Haram, S. K. Determination of Band Structure Parameters and the Quasi-Particle Gap of CdSe Quantum Dots by Cyclic Voltammetry. *ChemPhysChem* **2008**, *9* (17), 2574–2579. https://doi.org/10.1002/cphc.200800482.

(7) Maiti, S.; Dana, J.; Jadhav, Y.; Debnath, T.; Haram, S. K.; Ghosh, H. N. Electrochemical Evaluation of Dopant Energetics and the Modulation of Ultrafast Carrier Dynamics in Cu-Doped CdSe Nanocrystals. *J. Phys. Chem. C* **2017**, *121* (48), 27233–27240. https://doi.org/10.1021/acs.jpcc.7b10262.

(8) Haram, S. K.; Quinn, B. M.; Bard, A. J. Electrochemistry of CdS Nanoparticles: A Correlation between Optical and Electrochemical Band Gaps [5]. *J. Am. Chem. Soc.* **2001**, *123*, 8860–8861. https://doi.org/10.1021/ja0158206.

(9) Cao, Y.; Chen, J. J. J.; Barteau, M. A. Systematic Approaches to Improving the Performance of Polyoxometalates in Non-Aqueous Redox Flow Batteries. *J. Energy Chem.* **2020**, *50*, 115–124. https://doi.org/10.1016/j.jechem.2020.03.009.

(10) Deng, D.; Hao, C.; Sen, S.; Xu, C.; Král, P.; Kotov, N. A. Template-Free Hierarchical Self-Assembly of Iron Diselenide Nanoparticles into Mesoscale Hedgehogs. *J. Am. Chem. Soc.* **2017**, *139* (46), 16630–16639. https://doi.org/10.1021/jacs.7b07838.

Chapter 3 The Electrochemical Activities of Iron Diselenide Hedgehog Particles

3.1 Background and Approach

As described in Chapter 1, there are a lot of challenges to overcome in electrolyte systems. These challenges include dispersibility, resistance, adsorption, electrochemical and structural stability. Although we have built a suitable system for $FeSe_2$ HPs, we still need to conduct more electrochemical tests to demonstrate that these problems can be solved using the current electrolyte system. The dispersibility of the particles is important because active species need to be well-dispersed during different electrochemical courses. If particles tend to aggregate at the bottom, they cannot adsorb onto the surface of working electrode for activation and reaction.

The dispersion will maintain a small resistance as ions travel between the electrodes to maintain charge neutrality. Too large of a resistance will bring about connection issues and a low current response which will not accurately represent the electrochemistry happening in the electrolyte system due to the large overpotential needed to overcome the resistance. EIS tests are performed to investigate the resistance of the system.

The fundamental approach of all impedance methods is to apply a small amplitude sinusoidal excitation signal to the system under investigation and measure the response (current, voltage, *etc*.) A low amplitude sine wave $\Delta E\ sin(\omega t)$, of a particular frequency ω, is superimposed on the DC polarization voltage E_0. This results in a current response of a sine wave superimposed on the DC current $\Delta i\ sin(\omega t + \varphi)$. The current response is shifted with respect to the applied potential. The Taylor series expansion for the current is given by:

$$\Delta i = \left(\frac{di}{dE}\right)_{E_0,i_0} \Delta E + \frac{1}{2}\left(\frac{d^2i}{dE^2}\right)_{E_0,i_0} \Delta E^2 + ..$$

If the magnitude of the perturbing signal ΔE is small, then the response can be considered linear in first approximation. The higher order terms in the Taylor series can be assumed to be negligible. The impedance of the system can then be calculated using Ohm's law as: $Z(\omega) = E(\omega)/i(\omega)$. Characteristic *Z(ω)* is referred to as impedance; it is a complex quantity with a magnitude and a phase shift which depends on the frequency of the applied potential *ω*. In Cartesian coordinates, the impedance is given by: $Z(\omega) = Z'(\omega) - jZ''(\omega)$ where *Z'(ω)* is the real part of the impedance, *Z''(ω)* is the imaginary part, and $j = \sqrt{-1}$. The plot of the real part of impedance against the imaginary part is typically referred to as a Nyquist plot. While plotting data in the Nyquist format the real axis must be equal to the imaginary axis so as not to distort the shape of the curve. The shape of the curve is important in making qualitative interpretation of the data.[1,2]

The persistent adsorption of active species on the surface of the working electrode is not ideal for electrolyte systems since one would expect all available active species to be reacted on the electrode. This can be investigated by CV tests varying the scan rate and plotting the peak current (i_p) as a function of either the scan rate (v) or the square root of scan rate ($\sqrt{v}$).

In a CV system with reversible reactions where the active species adsorbed on the surface will be desorbed from the surface of the working electrode when the reaction complete,

$$i_p = (2.69 \times 10^5) n^{\frac{3}{2}} A C_O^* D_O^{\frac{1}{2}} v^{\frac{1}{2}} \ at\ 25℃$$

Where n is the number of electron transfers; A (cm^2) is the surface area of the working electrode; C_O^* (mol/cm^3) is the bulk concentration of the active species O; D_O (cm^2/s) is the diffusion coefficient of the active species. Thus, there should be a linear relationship between the peak current (i_p) and the square root of scan rate ($\sqrt{v}$, $(V/s)^{1/2}$).[1]

However, if the active species stays on the surface of electrode after reaction, other species are not able to access the surface, influencing the effective charge transfer. In this case for a Nernstian adsorbate layer, the peak current will be,

$$i_p = \frac{n^2F^2}{4RT} vA\Gamma_O^*$$

Where F = 96485 C/mol is the Faraday constant, R = 8.314 J/(K mol) is the ideal gas constant; T is the temperature, $A\Gamma_O^*$ is the moles of adsorbed O on the electrode surface. Hence, a linear relationship between the peak current (i_p) and the scan rate (v) can be observed.[1]

It is necessary to understand the redox processes. One should know what each peak refers to and what is the valence state changes during these reactions, assisted by other characterization methods such as X-ray Photoelectron Spectroscopy (XPS).

Electrochemical stability is crucial for the active species. Further electrochemical measurements including bulk electrolysis or electrocatalytic tests requires active species to react more intensively compared to a regular short term CV tests of 5 cycles. Thus it is important to look at electrochemical stability over a long reaction time. Meanwhile, one should also pay attention to the structure change for active species with nanostructure using electron microscopy.

3.2 Experimental

3.2.1 Chemicals

N,N-dimethylformamide (ACS reagent, ⩾99.8%), and lithium trifluoromethanesulfonate (LiTf, 99.95%, trace metals basis) were purchased from Sigma-Aldrich. $FeSe_2$ HPs were synthesized followed by the procedure mentioned in section 2.2.2.

3.2.2 Electrochemical Impedance Spectroscopy

A typical electrochemical impedance experimental setup consists of an electrochemical cell, a potentiostat, and a frequency response analyzer that applies the sine wave and analyses the response of the system to determine the impedance. We chose the most common set-up – a three-electrode system – for the EIS tests. Impedance is measured between the reference electrode and working electrode.[3] EIS tests were carried out by Autolab PGSTAT302N combined with Metrohm Autolab NOVA software to set up different procedures, record data, and give initial data analysis.

3.2.3 Scanning Electron Microscopy and Size Distribution

Scanning Electron Microscopy (SEM) was done using a FEI Nova 200 Nanolab Dualbeam/FIB System and a FEI Helios 650 Nanolab Dualbeam/FIB System. The size distribution was counted using ImageJ image editing software.

3.3 Results and Discussion

3.3.1 Dispersibility

In the Chapter 2, in order to fully utilize the potential of $FeSe_2$ HPs, a high concentration of 2 mg/mL $FeSe_2$ HPs was chosen to characterize the electrochemical activities of HPs. A dispersion of 2 mg/mL HPs is a dense slurry and would potentially have mass transport limitations if applied in the further studies. After rounds of preliminary examinations, an ideal concentration of 0.2 mg/mL was selected for further experimentation. In Figure 3-1, the 0.2 mg/mL dispersion is black with reasonable saturability, and light can still pass through the solution. In the first 30 minutes, precipitations were not seen at the bottom of the vial. After 30 minutes, $FeSe_2$ HPs started

to coagulate at the bottom. After 4 hours, although lots of HPs aggregated, some HPs were still dispersed in DMF as can be seen in Figure 3-1. This demonstrates that $FeSe_2$ HPs can maintain a good dispersibility for a relatively long time. Moreover, the particles stay suspended longer if stirring is introduced into the electrolyte system.

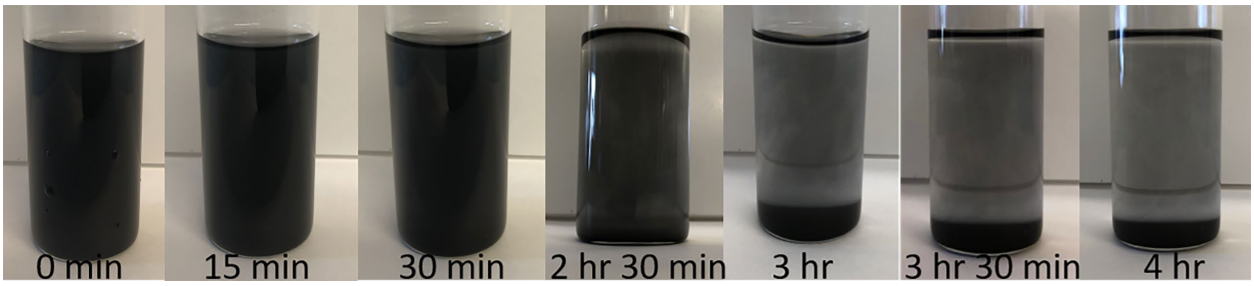

Figure 3-1 Digital images showing a 0.2 mg/mL $FeSe_2$ HPs dispersion in DMF in a vial from 0 mins to 4 hours.

3.3.2 Resistance

From EIS tests, the uncompensated resistance can be calculated. The uncompensated resistance (R_u) is the resistance between the surface of the working electrode and the tip of reference electrode. One can estimate the required overpotential using Ohm's Law. In our typical CV experiment, the current response usually has a magnitude of 10^{-6} A. If the overpotential is large, an *iR* compensation needs to be considered in order to get the corrected potential for all electrochemical test. Small overpotential can be safely neglected.[4]

In EIS experiments, one should choose a suitable equivalent circuit to represent the electrochemical system. The Randles circuit is one of the simplest and most common cell models. It includes an uncompensated resistance (solution resistance), a double layer capacitor and a double layer capacitance (polarization resistance) (Figure 3-2). For the electrolyte system of nanoparticles, it is also reasonable to add Warburg Impedance along with the charge transfer resistance to describe a system when both kinetics and diffusion are important. However, in any

case, the procedure to calculate R_u does not change, so it will be acceptable to use Randles Circuit to find the uncompensated resistance.[5]

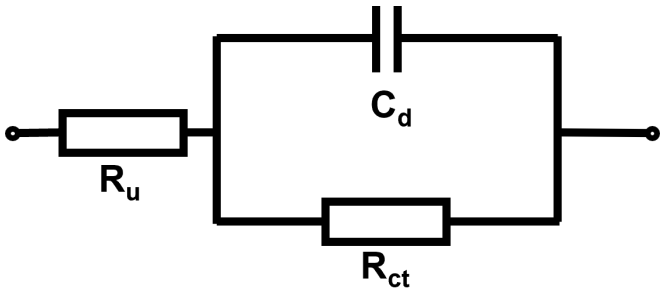

Figure 3-2 A diagram of Randles Circuit. R_u represents the uncompensated resistance. R_{ct} represents the charge transfer resistance. C_d represents the double layer capacitance.

Based on the Nyquist plot (Figure 3-3), the uncompensated resistance is the distance between the origin and the intercept of the semiconductor at the lower Z'(Ω) end (highest frequency), and the value is approximately 20 Ω. Considering an average current response of 1 μA in the CV tests with gold disk working electrode, the overpotential will be,

$$Overpotential = i \times R_u = 10^{-6}A \times 20\Omega = 2 \times 10^{-5}V = 0.02\ mV$$

Considering the potential range where CV tests were conducted, the overpotential of 0.02 mV can be safely neglected.

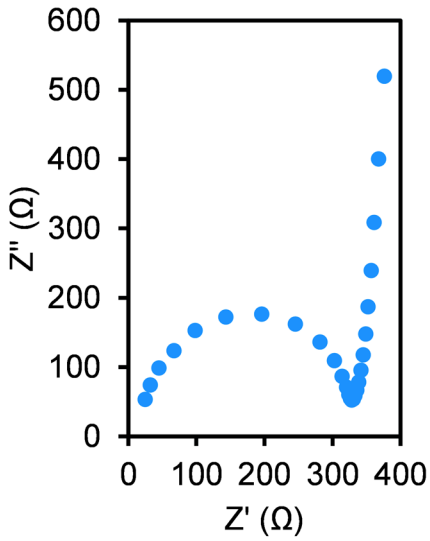

Figure 3-3 Nyquist plot of 0.2 mg/mL $FeSe_2$ HPs in DMF with 0.1 M LiTf (gold disk working electrode). Frequency sweep from 700 kHz to 1 Hz. Data from 700 kHz to 554 Hz are shown in the plot.

3.3.3 Adsorption

It is necessary to understand if active species are adsorbed on the surface of the working electrode. If they stay on the surface over entire electrochemical measurement, that can be problematic since other active species are not accessible to be activated. CV tests were performed by changing the scan rate from 100 mV to 50 mV and 25 mV. Since the potential is continuously changing in a CV experiment, a charging current (i_c), always flows.

$$|i_c| = AC_d v$$

In this equation, C_d is the double layer capacitance. Therefore, the peak current (faradaic current) must always be measured from a baseline of charging current and it is necessary to subtract the calculated charging current before plotting the peak current versus scan rate.[1]

In Figure 3-4, the oxidation peak current decreases as the scan rate decreases. By subtracting the charging current, there is clearly a linear relationship (R^2=1) between the oxidation

peak current and the square root of scan rate. Therefore, $FeSe_2$ HPs are unlikely to be adsorbed on the surface of the working electrode throughout the entire electrochemical measurement, and the charge transfer will not be affected by this reason.

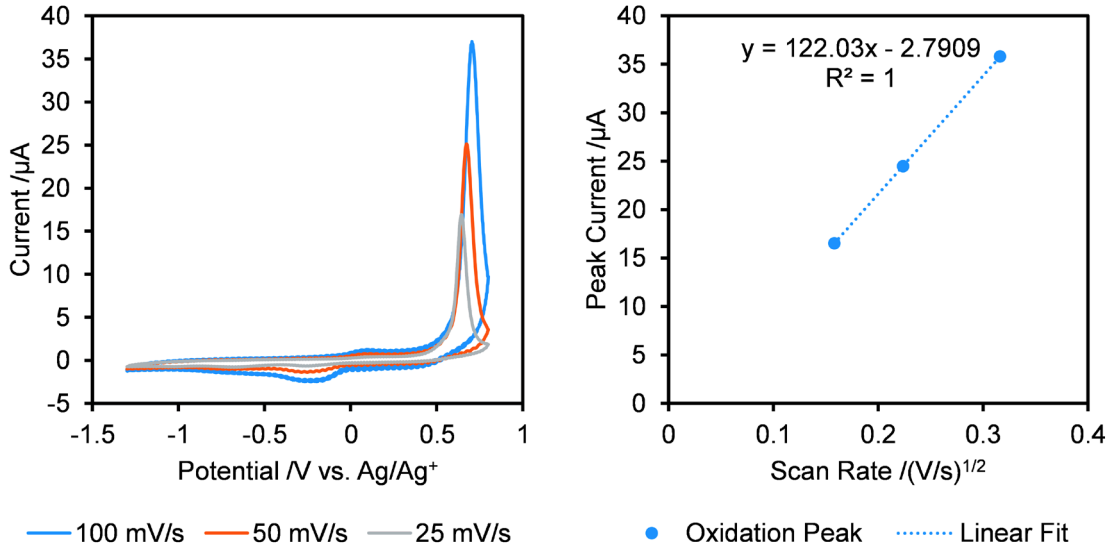

Figure 3-4 Left: CVs of 0.2 mg/mL $FeSe_2$ HPs in DMF with 0.1 M LiTf (gold disk working electrode). Scan rate of 25, 50, and 100 mV/s, 5th cycle. Right: Plot of peak current (i_p, μA) versus the square root of scan rate ($v^{1/2}$, $(V/s)^{1/2}$) in CV tests with different scan rates from 25 to 100 mV/s.

3.3.4 Redox Processes

It is important to understand the reaction by looking at the initial few cathodic and anodic scans. In Figure 3-5, no reduction peaks can be seen from the initial cathodic scan, meaning that $FeSe_2$ cannot be reduced in this potential range. But the oxidation peak appears during the initial anodic scan, which demonstrate the oxidation of $FeSe_2$ HPs in this region. Next, it is possible to observe reduction peak related of $FeSe_2$ HPs, which represents the reduction of previously oxidized $FeSe_2$ species.

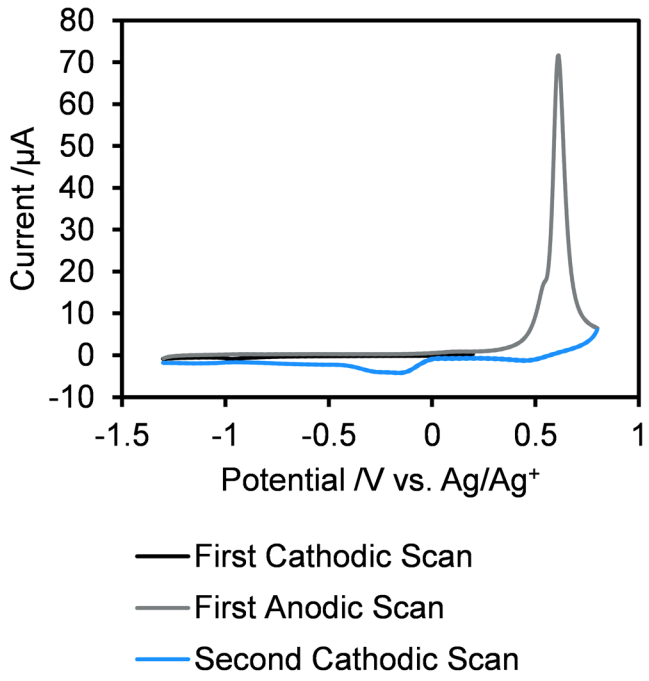

Figure 3-5 CVs of 0.2 mg/mL $FeSe_2$ HPs in DMF with 0.1 M LiTf (gold disk working electrode). Scan rate of 0.1 V/s. Potential initially scanned in the cathodic direction from 0.2 V to -1.3 V (black), along with the first anodic scan from -1.3 V to 0.8 V (gray) and the second cathodic scan from 0.8 V to -1.3 V vs. Ag/Ag^+ (blue).

It is possible to get the same results with the other similar experiments by varying the potential range (Figure 3-6). When CV scans were performed between -1.3 V to 0.2 V vs. Ag/Ag^+, no apparent peaks can be seen. However, if the span is expanded up to 0.8 V vs. Ag/Ag^+, both oxidation peak and reduction peak regarding $FeSe_2$ HPs show up. Therefore, both experiments demonstrate that $FeSe_2$ HPs can be oxidized at *ca.* 0.65 V vs. Ag/Ag^+ in that potential range.

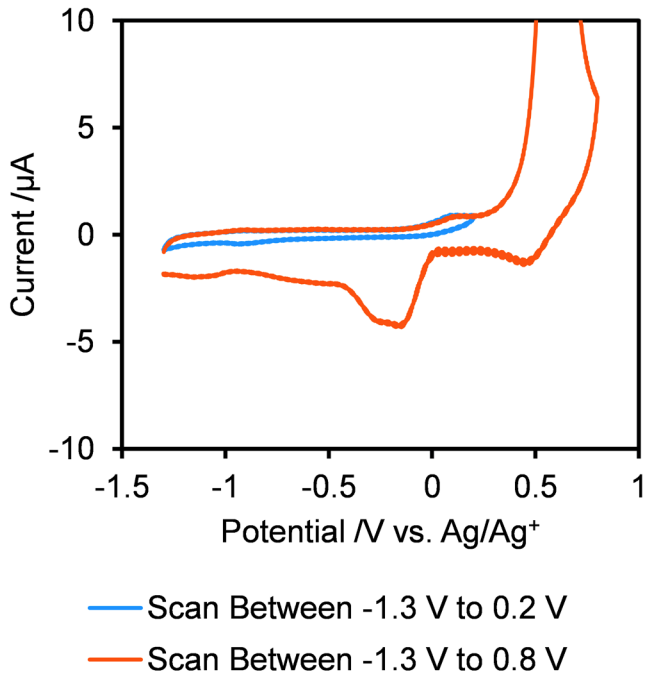

Figure 3-6 CVs of 0.2 mg/mL $FeSe_2$ HPs in DMF with 0.1 M LiTf (gold disk working electrode). Scan rate of 0.1 V/s. Blue: CV scan between -1.3 V to 0.2 V. Orange: CV scan between 1.3 V to 0.8 V.

3.3.5 Electrochemical and Structural Stability

For the purpose of investigating the long term electrochemical stability, a long-term CV experiments were conducted. As mentioned in section 3.3.1, $FeSe_2$ HPs can disperse in DMF for at least 4 hours. Thus, CV tests were extended to 250 cycles with a total cycling time of around 4 hours, and the CV curve from the 5^{th} cycle is compared with other CV curves all the way to the 250^{th} cycle.

From Figure 3-7, the intensity of the oxidation peak current gradually decreased by 30% by the 250^{th} cycle. This was due to the precipitation of $FeSe_2$ HPs at the bottom of the cell, which made less HPs available to be adsorbed on the surface of the working electrode. In other words, the actual concentration of HPs decreased because of the particle settling. Another thing is that the oxidation peak shifted slightly toward the positive direction. By looking at the CV with a different

scan rate (Figure 3-4), one can see that the position of the oxidation peak shifts to the positive side as the scan rate is increased. This phenomena implies that the oxidation reaction has some kinetic issues because reactions tend to occur more effectively with slow scans. Similarly in this scenario, as cycling continues and more HPs coagulate at the bottom of the cell, it is reasonable to expect a peak shift since the oxidation of HPs becomes harder to complete within the time of the single cathodic scan. The nanostructure can also play a role in the peak shift so it was necessary to look at the HPs after the long-term CV experiments.

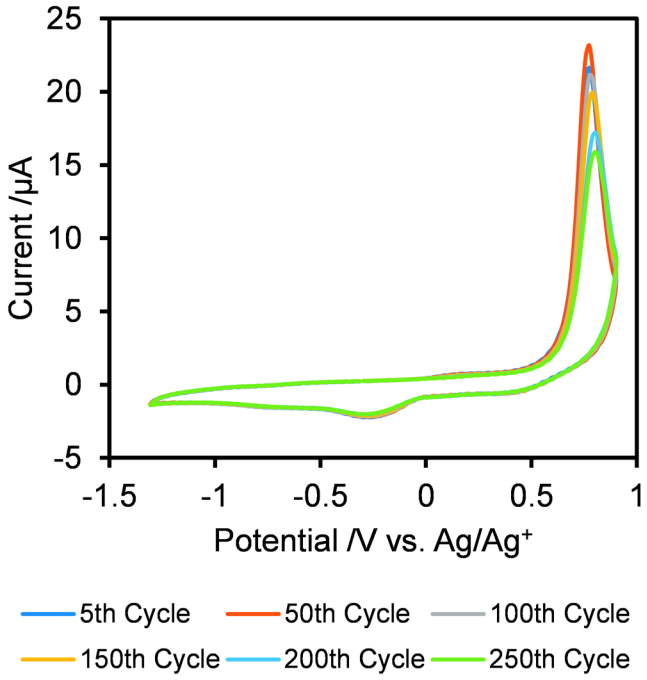

Figure 3-7 CVs of 0.2 mg/mL $FeSe_2$ HPs in DMF with 0.1 M LiTf (gold disk working electrode) for continuous cycling over 250 cycles taken for the 5th, 50th, 100th, 150th, 200th, and 250th cycles. Scan rate of 0.1 V/s.

Comparing SEM images from before and after the long-term CV tests, one can identify that generally the hedgehog structures stayed intact after the electrochemical treatment (Figure 3-8). This largely eliminates the possibility of a particle structure collapse, giving rise to the peak shift in Figure 3-7.

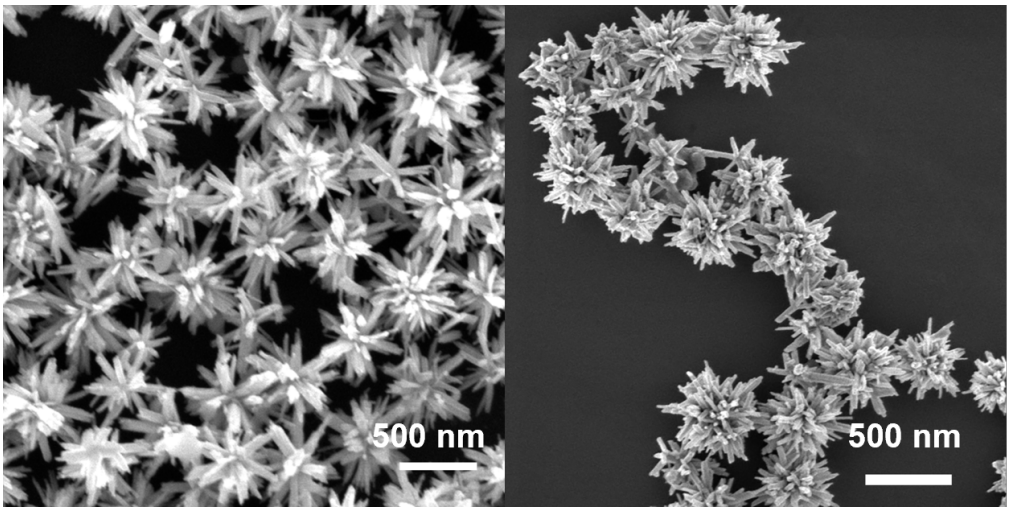

Figure 3-8 SEM images of $FeSe_2$ HPs as prepared (left) and after the long-term CV experiment (right).

100 HPs and 100 nanospikes on the HPs were counted analyzing data for Figure 3-9. The diameter of HPs decreased from 556 ± 40 nm to 551 ± 46 nm (-1%) and the length of nanospikes decreased from 276 ± 23 nm to 267 ± 26 nm (-3%). Although the numbers decreased in both categories, HPs still generally maintained their size after long-term CV experiments. More importantly, the particle dispersion is normally distributed after the test, which demonstrates good structural integrity throughout the electrochemical studies.

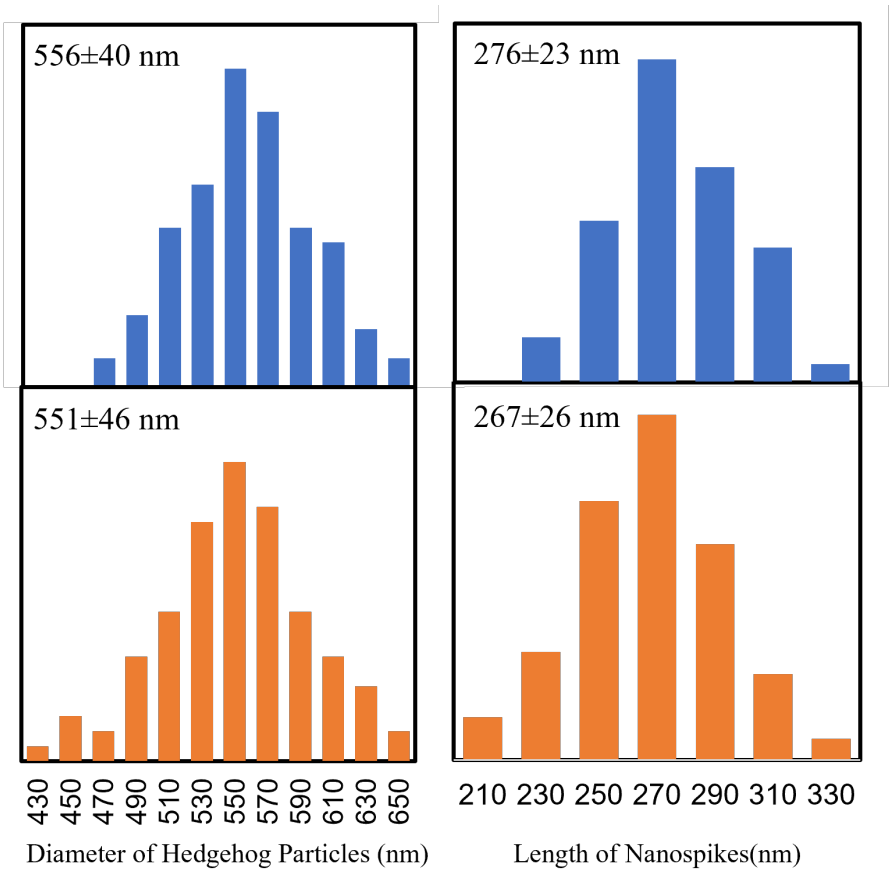

Figure 3-9 Comparison of the diameter of hedgehog particles and the length of nanospikes before (blue) and after (orange) the long-term CV experiments.

3.4 Conclusions

An electrolyte consisting of 0.2 mg/mL $FeSe_2$ HPs in DMF using a gold disk working electrode has a small resistance, and the uncompensated resistance can be safely neglected. Furthermore, CV of $FeSe_2$ HPs displayed an oxidation peak at *ca.* 0.65 V vs. Ag/Ag^+, proving that $FeSe_2$ can be oxidized in this range. During this reaction, HPs are adsorbed on the surface of gold disk working electrode and desorbed from the surface of working electrode when the oxidation reactions complete.

The electrolyte for the electrochemical studies was found where $FeSe_2$ HPs are not only highly dispersible but also electrochemically stable as demonstrated by long-term CV tests. The hedgehog structure (including the diameter of particle and the length of nanospikes) remained intact after the long-term CV tests as well.

3.5 References

(1) A.J. Bard; Faulkner, L. R. Electrochemical Methods: Fundamentals and Applications; John Wiley & Sons, Inc.: New York, **2001**.

(2) Electrochemical Impedance Spectroscopy (EIS) Part 1 – Basic Principles (Autolab Application Note EIS001); Metrohm Autolab B.V., **2011**.

(3) Electrochemical Impedance Spectroscopy (EIS) Part 2 - Experimental Setup (Autolab Application Note EIS 002); Metrohm Autolab B.V., **2011**.

(4) Electrochemical Impedance Spectroscopy (EIS) Part 3 - Data Analysis (Autolab Application Note EIS 003); Metrohm Autolab B.V., **2011**.

(5) Electrochemical Impedance Spectroscopy (EIS) Part 4 – Equivalent Circuit Models (Autolab Application Note 004); Metrohm Autolab B.V., **2011**.

Chapter 4 The Charging Capacity of Iron Diselenide in the Electrolyte System

4.1 Background and Approach

The amount of charge that can be stored on a particle without their chemical or physical degradation is the essential attribute of an electroactive colloidal species that allows particles to be compared to the oxidation/reduction state of molecules.

Theoretically, multiple methods including CV[1] can be applied to calculate the charging capacity. The current voltage curve from rotating disk electrode (RDE) which improves the mass transport is a reliable option to get the charge capacity from the Levich Equation[2]. However, all methods required estimation of some parameters, like the diffusion coefficient, in the equation. Moreover, the electrochemical properties of electroactive colloidal species may not fully comply with the rules that were frequently tested by electrochemical systems of small molecules. Thus, it is crucial to find a universal way to investigate the charging capacity.

It is believed that bulk electrolysis can be used for any electroactive colloidal species. Bulk electrolysis experiments are carried out as a potential step experiment and can determine the number of charge transfers of electroactive colloidal species in the cell. The colloidal dispersion is either reduced or oxidized stepwise for a fixed amount of charge at each step. In principle, all the electroactive species that can react will react in that certain region, generating charges to reach the charge cut-off. Bulk electrolysis experiments are not affected by the mass transport of active species if a high surface area working electrode is applied for electroactive colloidal particles to react on. SEM images comparing the hedgehog structure before and after the bulk electrolysis experiment can give more information about the structural integrity of HPs.

The concentration of HPs was measured by NTA because this method is very suitable for colloidal particles in size range from nanometers to microns. HPs are also convenient for this technique due to their high refractive index. By carefully conducting NTA experiments to calculate the particle concentration, one can easily convert the charges from bulk electrolysis to the charging capacity of the active species. It is also possible to compare the capacity with other previously studied electroactive colloidal species in many aspects including charges per surface area and per volume of a single particle, charges per crystal unit cell, and charges per surface area of working electrode at the peak potential.

Although the charge capacity can be calculated by bulk electrolysis, it is important to validate the results by conducting computational simulations as well. Here, the lattice dynamics of $FeSe_2$ HPs with different amounts of charges by phonon dispersion using Density Functional Perturbation Theory (DFPT) calculations along the high-symmetry lines in the Brillouin zone were performed by the collaborator Dr. Bingcheng Luo.

It is important to investigate the valence changes of both Selenium and Iron atoms since the results will tell the activities of these elements during bulk electrolysis. Therefore, XPS experiments were performed to grasp what is happening through the electrochemical experiments.

4.2 Experimental

4.2.1 Chemicals

N,N-dimethylformamide (ACS reagent, ⩾99.8%), and lithium trifluoromethanesulfonate (LiTf, 99.95%, trace metals basis) were purchased from Sigma-Aldrich. $FeSe_2$ HPs were synthesized followed by the procedure mentioned in section 2.2.2.

4.2.2 Bulk Electrolysis

Bulk electrolysis experiments were controlled with the PGSTAT302N Potentiostat (Metrohm Autolab USA). In this experiment, the working electrode was held at 1.0 V vs. Ag/Ag^+ (reference electrode, MF-2062, BASi), below the higher limit for the solvent in order to maintain a maximum driving force. The working electrode applied here was a homemade gold-coated reticulated vitreous carbon (RVC) electrode because there were not commercially available highly porous gold electrodes. Therefore, we used the SPI Sputter Coater (Michigan Center for Materials Characterization, $(MC)^2$) to coat the RVC electrode (45 Pores Per Inch (PPI), Low Flow, McMaster Carr, previously cut into thin piece) for 120 seconds on each side. After the coating, the as-fabricated working electrode was dried in air overnight before use. All bulk electrolysis experiments were performed at 25 °C in a glove box. The platinum coil counter electrode (MW-1033, BASi) in the bulk electrolysis test was used to measure the current.

In the bulk electrolysis experiments, 0.3 mg/mL $FeSe_2$ HP dispersion was oxidized stepwise for a fixed amount of charge at each step. At the end of each charge, the experiment was paused for 15 seconds to rest and measure the open circuit potential (OCP) for 15 seconds. This allows the system to return to a state with no current. The experiment was stopped when the experiment was slow due to a small driving force. The amount of charge transferred can be calculated at any point.

4.2.3 Density Functional Perturbation Theory (by the Collaborator Dr. Bingcheng Luo)

The calculations were performed by using a density functional theory (DFT) framework in a Vienna ab initio simulation program (VASP)[3-5]. $FeSe_2$ had a Pmnn space group with the lattice parameter a = 3.58 Å, b = 4.79 Å and c = 5.74 Å for one formula unit per unit cell. $FeSe_2$ crystal structures with a 2×2×1 supercell was built to perform the optimization and properties calculations. Same conclusions were further validated by repeated calculations using 2×1×1 supercell and 1×1×1 supercell. We employed the generalized gradient approximation (GGA) functional with the Perdew−Burke−Ernzerhof for solid (PBEsol). Full geometry optimization was performed until reaching the convergence criteria: the Hellmann−Feynman force component on each atom was less than 0.001 eV/Å and total energy was less than 1×10^{-8} eV. The effects of charging were simulated through the excess electron doping on $FeSe_2$ supercell. We employed a kinetic energy cutoff of 600 eV and an automatically generated 4 × 3× 4 Monkhorst−Pack set of k points. The pseudopotentials were constructed by the electron configurations as Fe $3d^6$ $4s^2$ states and Se $4s^2$ $4p^4$ states. The phonon dispersion and other lattice vibration properties were carried out using DFPT methods through phonopy[6] and phono3py[7] package.

4.2.4 Other Characterizations

XPS experiments were performed in a Kratos Axis Ultra XPS (at $(MC)^2$ of University of Michigan). As-prepared $FeSe_2$ HPs samples were powder. $FeSe_2$ HPs after bulk oxidation were dispersed, and a few droplets of the dispersion were deposited onto the surface of silicon wafer and allowed to air dry. All samples were fixed on copper tape attached to the bar, and the bar was transferred from Sample Transfer Chamber (STC) to Sample Analysis Chamber (SAC) for measurement. The working power set-up for these tests were 14 kV HT and 8 mA Emission, and all tests were done at room temperature. After the test, all peaks were calibrated using the signature

C 1s peak located at 285 eV to generate the Se 3d XPS and Fe 2p XPS spectra. I note that XPS tests cannot be performed in-situ, so all the samples need to be removed from the glove box and transferred to the STC. The samples will be exposed in air for a short period of time, therefore the minor oxidation under atmosphere cannot be avoid.

NTA were operated using Malvern NanoSight NS300 (Malvern Panalytical, UK) and 405 nm violet laser module was selected. NTA tests were carried out in Nanotechnicum at UM Biointerface Institute (biointerfaces.umich.edu). Due to the limitation of instrument requirement, 0.05 mg/mL $FeSe_2$ HPs were dispersed in ultra-purified water for NTA experiments.

4.3 Results and Discussion

4.3.1 Bulk Electrolysis

The bulk electrolysis can determine the quantity of charge transfers in the dispersion throughout the course of charging. From Figure 4-1, the dispersion of $FeSe_2$ HPs can store up to 0.5 C during bulk oxidation. When comparing with the CV of $FeSe_2$ HPs in DMF (Figure 3-5), charging occurs in the same potential range as the oxidation of $FeSe_2$ HPs, meaning that the charge stored on $FeSe_2$ HPs is due to the oxidation reaction.

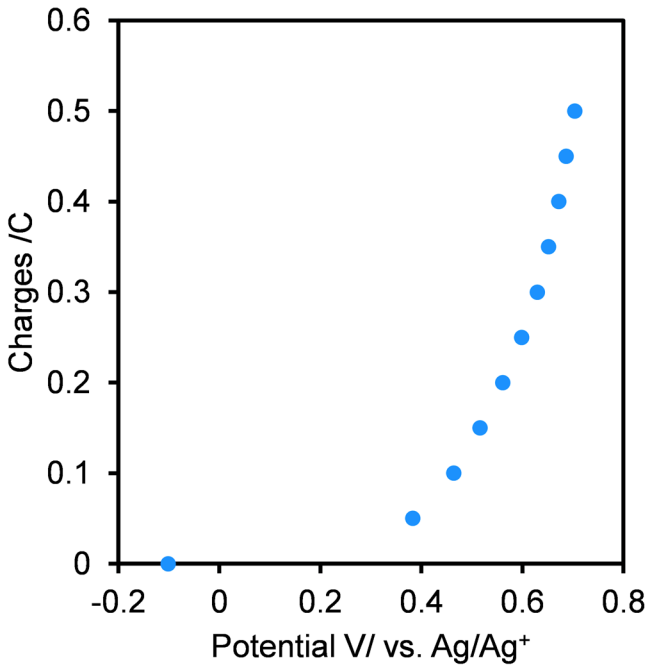

Figure 4-1 Bulk electrolysis plot of $FeSe_2$ HPs in DMF.

To calculate the particle concentration of HPs, NTA experiments were applied. Due to the high sensitivity of the technique and optical thresholds of the instrument, highly diluted solutions are used. Thus, for NTA tests, we dispersed 0.75 mg $FeSe_2$ HPs in 15 mL ultra-purified water. Note that $FeSe_2$ HPs were in water instead of DMF due to the instrumental limitation, but it does not affect the result in determination of particle concentration. Here, $c_{FeSe2\ HPs}$ = 7.5 mg/15 mL=0.05 mg/mL.

From NTA measurements, one can get the particle concentration is $(6.6 \pm 0.11) \times 10^8$ particle/mL, which translates into $\frac{((6.6\pm0.11)\times10^8)\ \text{particle/mL}}{6.02\times10^{23}\text{particle/mol}^{-1}} = (1.1 \pm 0.02) \times 10^{-15}$ mol cm^{-3}

So, the averaged molar mass of HP ($M_{FeSe2\ HP}$) is

$$M_{FeSe2\ HP} = \frac{0.05\ \text{mg cm}^{-3}}{1.1 \times 10^{-15}\text{mol cm}^{-3}} = 4.6 \times 10^{10}\text{g mol}^{-1}$$

Considering $M_{FeSe2} = 213.77\ g/mol$

$$N_{FeSe2} = 4.6 \times 10^{10}/213.77 = 2.2 \times 10^8$$

Therefore, an average of 2.2×10^8 $FeSe_2$ crystalline unit cells are in a single HP.

From the bulk electrolysis experiment results,

$$n = \frac{q/F}{c_{FeSe2} \times V/M_{FeSe2}} = 0.7$$

an average of 0.7 charges can be charged per $FeSe_2$ crystalline unit cell.

Thus, the number of charges stored per $FeSe_2$ HPs will be

$$N = 0.7 \times 2.2 \times 10^8 = 1.54 \times 10^8$$

The surface area of a single HP is 6.6×10^6 nm^2. The surface area of a single HP includes both core and scrolls. The core diameter is 4 nm. There is an average of 200 nanospikes on a single HP. The outer diameter of the scroll is 22 nm and the thickness of the scroll is 3 nm on average. Considering a particle with same surface area charged from OCP of -0.1 V to 0.7 V vs. Ag/Ag^+, the total amount of charges due to the capacitive effect will be ~ 3.3×10^6 (or 0.5 $/nm^2$). Therefore, 98% of charges stored on the $FeSe_2$ HP are related to the oxidation of HPs in the bulk electrolysis experiment.

Please note that $FeSe_2$ HPs can also be oxidized on the surface of the glassy carbon working electrode (Figure 2-2) in this potential range since the gold coated RVC electrode was applied in the bulk electrolysis experiment, therefore this test tends to overestimate the actual charges due to the oxidation on the glassy carbon working electrode. But, considering the relatively small oxidation peak current of $FeSe_2$ HPs on the glassy carbon working electrode, this will not significantly change the number of charges that can be stored on HPs.

4.3.2 Lattice Dynamics of $FeSe_2$ HPs with Different Number of Charges (by the Collaborator Dr. Bingcheng Luo)

We decided to assess the lattice dynamics of $FeSe_2$ HPs with different amounts of charges by phonon dispersion using DFPT calculations along the high-symmetry lines in the Brillouin zone. The total number of valence electrons (N_e) for uncharged Fe_8Se_{16} with no excess charges was 160 per unit of 2×2×1 supercell. All frequencies were positive values. Note that emergence of imaginary phonon frequencies indicates the thermodynamic instability. When excess charges of 1 to 4 were introduced in Fe_8Se_{16} supercell, these structures remained thermodynamically stable (Figure 4-2). When 5 charges were introduced in Fe_8Se_{16} supercell (N_e=155), imaginary phonon frequencies appeared in the high-symmetry lines in the Brillouin zone, indicating that the structure became thermodynamically unstable (Figure *4-2*).

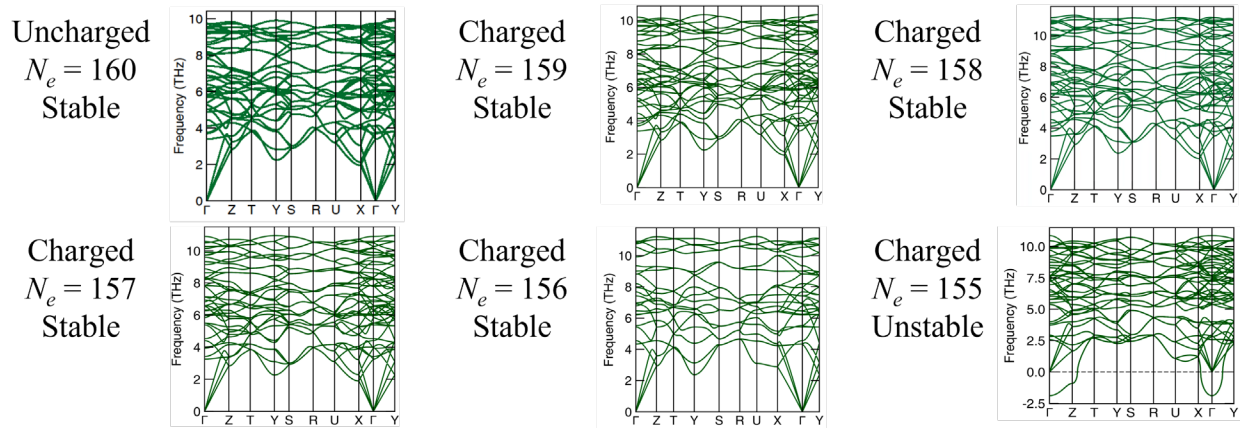

Figure 4-2 Phonon dispersion relations of $FeSe_2$ with different amounts of excess charges. N_e represents the total valence electrons per unit of supercell. N_e=160 for uncharged Fe_8Se_{16}. When N_e=155, the bulk becomes unstable. (By the collaborator Dr. Bingcheng Luo)

If you apply the experimental results of $FeSe_2$ HPs in section 4.3.1 (0.7 charges per $FeSe_2$ crystalline unit cell) to the Fe_8Se_{16} supercell, Fe_8Se_{16} supercell should be able to store an excess of 5.6 charges. Considering the overestimation due to the oxidation of $FeSe_2$ HPs on the surface of carbon working electrode, the experiment data fit well with the DFPT calculation results, displaying the large charging capacity of $FeSe_2$ HPs in the electrolyte system.

4.3.3 Comparison of Charging Capacity (Partly by the Collaborator Dr. Bingcheng Luo)

While there was no previous research on charging capacity of HPs or similar colloidal particles with complex geometries, the presented data can be compared with the electron charging capacity reported for semiconductor nanoscale colloids or quantum dots studied in the electrolyte system before.

According to *Electrochemical Methods Fundamentals and Applications Second Edition* page 231[8], the peak current in CV curves, for reversible reactions can be represented as

$$i_p = (2.69 \times 10^5) n^{3/2} A D_O^{1/2} C_O^* v^{1/2};$$

while the peak current for irreversible reactions (page 236)

$$i_p = (2.99 \times 10^5) \alpha^{1/2} A D_O^{1/2} C_O^* v^{1/2}.$$

In the CV system of $FeSe_2$ HPs, we can measure the number of charge transfers $N = 1.5 \times 10^8$, the surface area of the working electrode $A = 0.071\ cm^2$, the diffusion coefficient (obtained by Dynamic Light Scattering (DLS) experiments) $D = 7.93 \times 10^{-9}\ cm^2 s^{-1}$, the bulk concentration of $FeSe_2$ HPs $C^* = 4.36 \times 10^{-15} mol\ cm^{-3}$ (converted from data collected by NTA experiments), and the scan rate $v = 0.1\ V/s$. For most irreversible reactions, α is between 0.3 to 0.7, and thus we can assume that $\alpha \sim 0.5$.[8]

Comparing the theoretical peak currents to experimental ones, the reversible equation is better for estimating the peak current in the CV system of $FeSe_2$ HPs. We used the same equation used in the CV system of $FeSe_2$ HPs to estimate the charging capacity of CdS NP. Based on the number of electron passages of 50 at the peak potential per CdS NP reported by Haram *et al.*[1], the number of charges stored per CdS unit cell is ~0.01, which is about 70 times less than for $FeSe_2$ HPs.

When considering the charges per surface area of a single particle, $FeSe_2$ HPs surpassed other studied nanoparticles[1,2] by more than an order of magnitude. This echoes the conclusion drawn in Chapter 1 that nanostructures with higher surface roughness tend to improve the electrochemical properties since nanoscale surface features may increase the surface charge density. Compared with spherical semiconductor NPs studied before with no surface corrugation, HPs coated with high aspect ratio nanospikes will give rise to field concentration effects at the nanoscale apexes and generate a high charge capacity as a result.

Table 4-1 Comparison of charges per surface area of a single particle.

Particles	$FeSe_2$ HPs	CdS NPs[1]	CdS Colloidal Semiconductor[2]
Charges	1.5×10^8	50	270
Surface Area (nm^2)	6.6×10^6	50	201
Charges per Surface Area ($1/nm^2$)	17	1	1.3

Note: the surface area of a HP includes both core and scrolls. The core diameter is 4 nm. There is an average of 200 nanospikes on a single HP. The outer diameter of the scroll is 22 nm and the thickness of the scroll is 3 nm on average.

In the aspect of charges per volume of a single particle, $FeSe_2$ HPs outperformed others by an order of magnitude (Table 4-2). This again agrees with another conclusion in Chapter 1 that nanostructures with complex geometric features tend to improve the electrochemical performance. Comparing to spherical semiconductor NPs, HPs have a much more complex shape that will amplify anomalous charge transport dynamics and lead to an improvement in charging capacity.

Table 4-2 Comparison of charges per volume of a single particle.

Particles	$FeSe_2$ HPs	CdS NPs[1]	CdS Colloidal Semiconductor[2]
Charges	1.5×10^8	50	270
Volume (nm^3)	9.9×10^6	34	268
Charges per Volume ($1/nm^3$)	15	1.5	1

Note: the volume of a HP includes both volume of the core and scrolls. The core diameter is 4 nm. There is an average of 200 nanospikes on a single HP. The outer diameter of the scroll is 22 nm and the thickness of the scroll is 3 nm on average.

In terms of charges per surface area of working electrode at peak potential, one can compare the electrolyte system of $FeSe_2$ HPs with other electrolytes used for semiconductor NP dispersions[1,9,10] and other electrode systems where $FeSe_2$ or other nanoscale or microscale semiconductor materials were used as an electrode or immobilized on the electrode surface[11-19].

Due to the various experimental setups from other research projects, it was crucial to make sure that the comparison was based on the same criteria. Therefore, the value of charges per surface area of the working electrode are compared considering the different electrodes' surface area and scan rate applied in each studies. Also, it is important to use the appropriate equation to estimate the values of charges in order to draw a sound conclusion (Table 4-3). If all of these factors are considered, the calculated charges per surface area of working electrode at peak potential of $FeSe_2$ HPs is still large relative to other electrolyte systems. The calculated number of $FeSe_2$ HPs is smaller than that of other electrode systems but their application still looks very promising considering the larger concentration of active species on the surface of the working electrode in those systems. Overall, this work shows the excellent electrochemical activities of $FeSe_2$ HPs on the surface of the gold disk working electrode.

Table 4-3 Comparison of charges per surface area of working electrode at peak potential.

Category	Title	Charge per surface area (paper, C/cm^2)	Charge per surface area ($FeSe_2$, C/cm^2)
Electrolyte	CdS NPs[1]	3.2×10^{-7}	3.6×10^{-6}
	CdTe QDs[9]	4.8×10^{-6}	5.1×10^{-6}
	CdTe NPs[10]	1.0×10^{-6}	3.2×10^{-6}
Electrode	$FeSe_2$ microspheres embedded into S-doped RGO sheets as anode for Na-ion batteries[11]	1.3×10^{-7}	2.3×10^{-5}
	3D porous carbon embedded with $FeSe_2$ as anode for Na-ion or Li-ion batteries[12]	3.2×10^{-4}	2.3×10^{-5}
	FeS_2@$FeSe_2$ microsphere as anode for Na-ion battery[13]	4.8×10^{-4}	6.3×10^{-5}
	Carbon-coated $FeSe_2$ nanosphere decorated RGO hybrid nanofiber as anode for Na-ion batteries[14]	1.0×10^{-4}	1.4×10^{-5}
	$FeSe_2$ microspheres as anode for Na-ion batteries[15]	9.6×10^{-4}	5.1×10^{-5}
	VS_2 nanosheet as cathode for Zi-ion battery[16]	4.8×10^{-4}	5.1×10^{-5}
	Sb_2S_3@FeS_2 nanorods anode for Na-ion batteries[17]	3.8×10^{-5}	1.6×10^{-5}
	Nano-MnO_2@TiO_2 microspheres as anode for Li-ion batteries[18]	1.8×10^{-4}	1.6×10^{-5}
	CdSe NP on gold microelectrodes[19]	5.0×10^{-5}	2.3×10^{-4}

In the 2×2×1 Fe_8Se_{16} supercell, a = 7.16 Å, b = 9.58 Å and c = 5.74 Å. (Figure 4-3) With charges introduced into the supercell, b and c remained stable. A remained stable with less than 3 positive charges introduced. A decreases by more than 10% when more than 4 charges are stored in the structure. Generally, the hedgehog structure can keep stable during bulk oxidation, due to minor atom displacement and small changes in bond lengths. Microscopic images before and after the electrochemical course are also valuable to demonstrate the structural integrity in the macroscopic view.

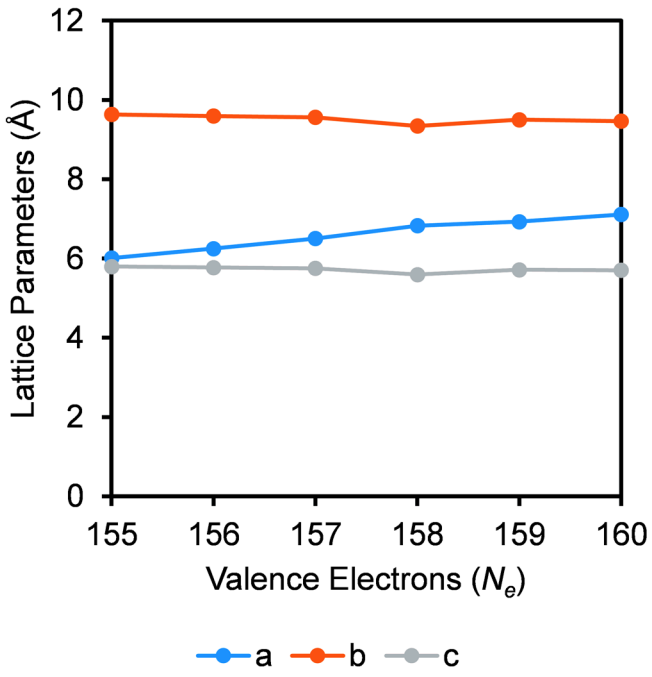

Figure 4-3 The changes of lattice parameters upon introduction of charges into the Fe_8Se_{16} supercell. (By the collaborator Dr. Bingcheng Luo)

4.3.4 Structural Change After Bulk Electrolysis

SEM images were taken after the bulk electrolysis experiment to compare with the digital images of as-prepared $FeSe_2$ HPs (Figure 3-8 Left). The overall structure remained but it was possible to see that size uniformity was sacrificed since smaller HPs are seen within the image (Figure 4-4).

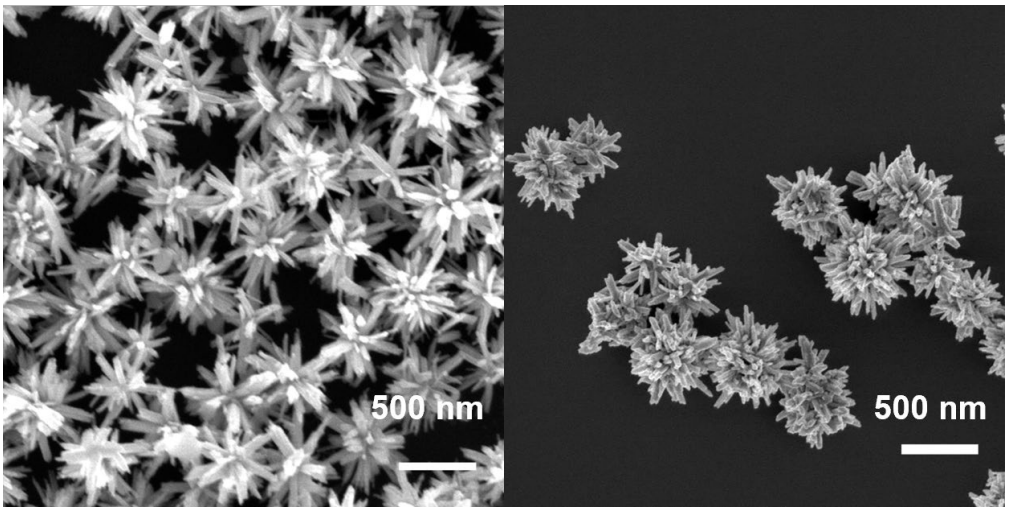

Figure 4-4 SEM images of $FeSe_2$ HPs as prepared (left) and after bulk electrolysis experiment (right).

The diameter of HPs and the length of nanospikes were compared in a similar way as described in Chapter 3. The diameter of HPs decreased from 556 ± 40 nm to 531 ± 51 nm (-4%) and the length of nanospikes decreased from 276 ± 23 nm to 262 ± 28 nm (-5%). Compared with the results after long-term CV experiments, both numbers decreased more after bulk electrolysis. This is due to the more intensive bulk electrolysis tests where all the available active species are reacted during the experiment. More importantly, however, the hedgehog structure did not collapse into other forms (nanoscrolls, sheets, bulks, *etc.*) after the experiments, indicating a good structural integrity of HPs.

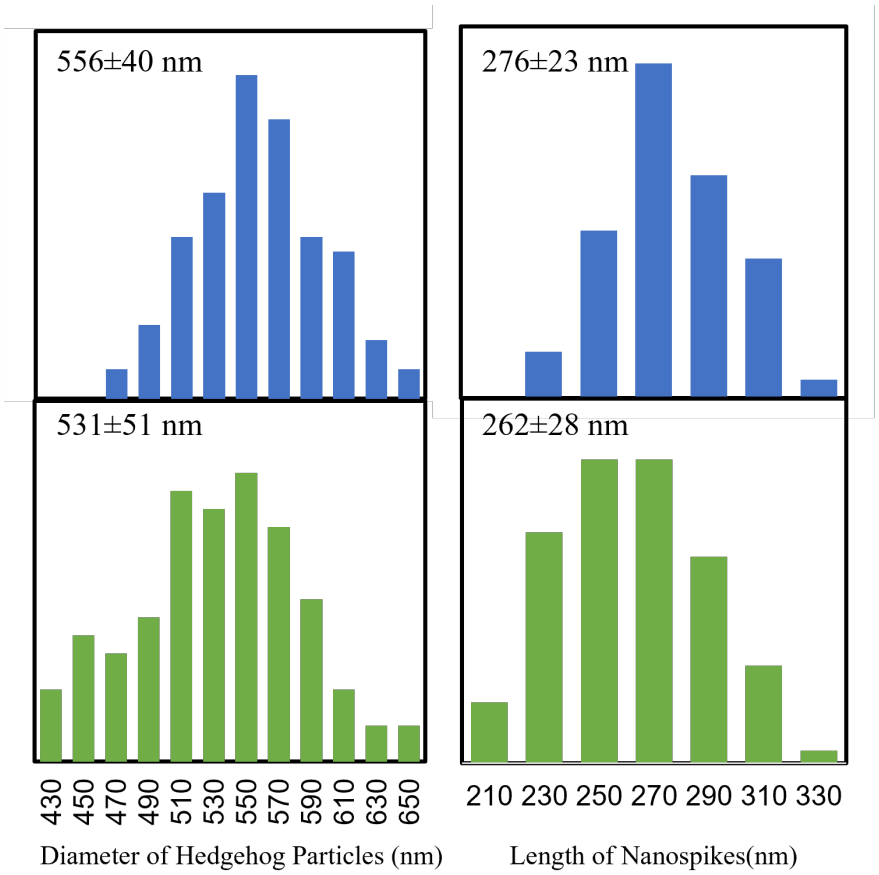

Figure 4-5 Comparison of the diameter of hedgehog particles and the length of nanospikes before (blue) and after (green) the bulk electrolysis experiments.

Table 4-4 Comparison of the average diameter of hedgehog particles and the average length of nanospikes before and after the long-term CV experiments and after the bulk electrolysis experiments.

$FeSe_2$ HPs	Diameter of Hedgehog Particles (nm)	Change	Length of Nanospikes (nm)	Change
As Prepared	556 ± 40	0	276 ± 23	0
After Long-term CV	551 ± 46	-1%	267 ± 26	-3%
After Bulk Oxidation	531 ± 51	-4%	262 ± 28	-5%

4.3.5 Valence Changes During Bulk Electrolysis

XPS of various $FeSe_2$ HPs helps us understand the valence changes during electrochemical measurements. Se 3d XPS spectra in Figure 4-6 displayed a peak at 57.6 eV that was attributed to Se atoms bonded with oxygen (Se-O bond); it corresponds to the surface oxidation state of selenium species ascribed to the high surface activities as building blocks commonly seen in many 3D $FeSe_2$ nanostructure.[20] The other two peaks in XPS spectra at 54.0 eV ($3d_{3/2}$) and 53.1 eV ($3d_{5/2}$) originated from spin orbit splitting Se 3d states with peak separation of less than 1 eV.

When the $FeSe_2$ HPs were charged to 0.7 V vs. Ag/Ag^+ in the bulk electrolysis experiment, both Se $3d_{3/2}$ and Se $3d_{5/2}$ peaks shifted about 2.5 eV higher in binding energy, meaning that selenium atoms will be oxidized during the bulk oxidation. Because these peaks are similar in binding energy to the Se-O peak, it was not clear if Se-O still existed. It is likely that selenium atoms are oxidized to a similar oxidation state as selenium species in the Se-O peak.

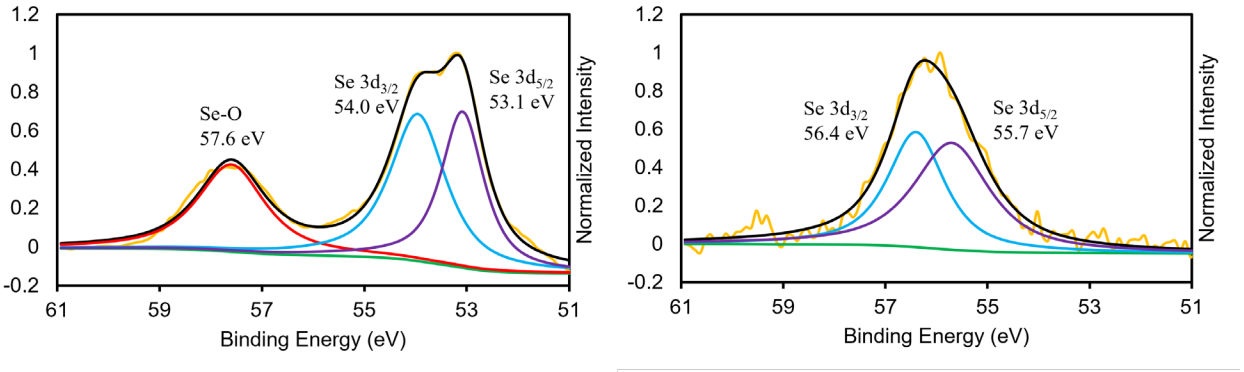

Figure 4-6 Se 3d XPS spectra of $FeSe_2$ HPs (left) and $FeSe_2$ HPs charged to OCP of 0.7 V vs. Ag/Ag^+ by bulk electrolysis experiments (right). Legends: Black - peak sum; Green - background; Red - peak 1 (Se-O); Blue - peak 2 (Se $3d_{3/2}$); Purple - peak 3 (Se $3d_{5/2}$); Yellow - raw intensity.

Original Fe 2p XPS spectrum contained four peaks, including signature $2p_{1/2}$ (718.4 eV) and its satellite peak (723.9 eV) and $2p_{3/2}$ (705.5 eV) peak and its satellite peak (710.0 eV). The spin separation of Fe 2p was 12.9 eV, exhibiting characteristics of divalent iron.[13] The satellite peaks may indicate the existence of a higher oxidation state of iron present in the $FeSe_2$ HPs.[21] For Fe 2p spectra obtained upon charging $FeSe_2$ HPs to 0.7 V vs. Ag/Ag^+ during bulk electrolysis

experiments compared to the original spectrum, the Fe $2p_{3/2}$ peak and its satellite peak shifted to the higher binding energy direction for 2 eV but the Fe $2p_{1/2}$ peak did not shift. Therefore, the peak separation reduced to 10.7 eV. This may indicate the oxidation of iron atoms due to the presence of divalent iron in $FeSe_2$ HPs. However, iron atoms were not oxidized on a large scale because the Fe $2p_{1/2}$ peak remained in the same location.

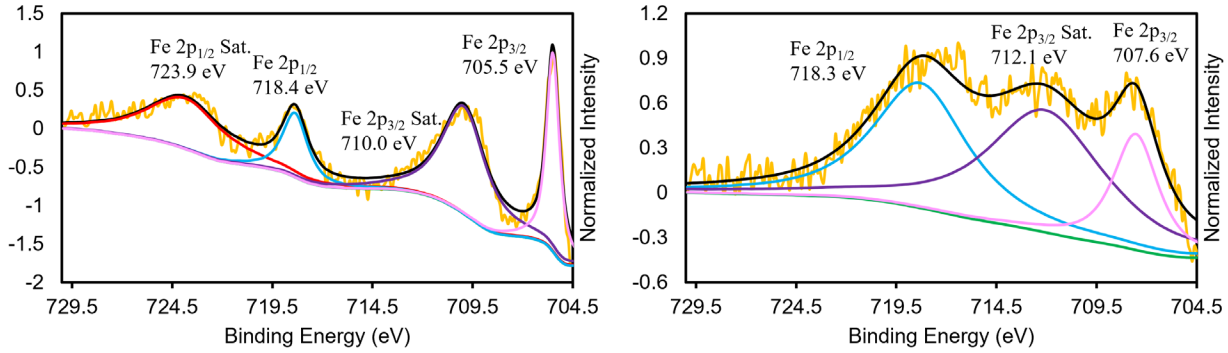

Figure 4-7 Fe 2p XPS spectra of FeSe2 HPs (left) and $FeSe_2$ HPs charged to OCP of 0.7 V vs. Ag/Ag^+ by bulk electrolysis experiments (right). Legends: Black - peak sum; Green - background; Red - peak 1 (Fe $2p_{1/2}$ sat.); Blue - peak 2 (Fe $2p_{1/2}$); Purple - peak 3 (Fe $2p_{3/2}$ sat.); Pink – peak 4 (Fe $2p_{3/2}$); Yellow - raw intensity.

4.4 Conclusions

$FeSe_2$ HPs displayed a huge charge capacity in the electrolyte system, with a maximum capacity of storing 1.5×10^8 charges per HP (or 0.7 positive charges per $FeSe_2$ crystalline unit cell). This significantly surpasses other previously studied semiconductor nanoparticles in many aspects including per crystal unit cell, per surface area, and per volume of a single particle owing to the high surface corrugation and complex geometry of HPs.

Furthermore, in the comparison of charges per surface area of the working electrode at peak potential with other nanoscale and microscale particles, HPs not only outperform semiconductor NPs without corrugation but also are only one order of magnitude behind other particles deposited on the surface of working electrode, which demonstrates the exceptional

electrochemical activities of HPs on the gold disk working electrode. When considering valence changes during bulk oxidation, mostly selenium atoms will be oxidized; iron atoms can be oxidized as well from the XPS spectra.

4.5 References

(1) Haram, S. K.; Quinn, B. M.; Bard, A. J. Electrochemistry of CdS Nanoparticles: A Correlation between Optical and Electrochemical Band Gaps. *J Am. Chem. Soc.* **2001**, *123*, 8860–8861. https://doi.org/10.1021/ja0158206.

(2) Albery, W. J.; Bartlett, P. N.; Porter, J. D. The Electrochemistry of Colloidal Semiconductor Particles: Experiments on CdS and TiO2. *J. Electrochem. Soc.* **1984**, *131* (12), 2896–2900. https://doi.org/10.1149/1.2115438.

(3) Kresse, G.; Furthmüller, J. Efficient Iterative Schemes for Ab Initio Total-Energy Calculations Using a Plane-Wave Basis Set. Phys. Rev. B - *Condens. Matter Mater. Phys.* **1996**, *54* (16), 11169–11186. https://doi.org/10.1103/PhysRevB.54.11169.

(4) Blöchl, P. E. Projector Augmented-Wave Method. *Phys. Rev. B* **1994**, *50* (24), 17953–17979. https://doi.org/10.1103/PhysRevB.50.17953.

(5) Joubert, D. From Ultrasoft Pseudopotentials to the Projector Augmented-Wave Method. Phys. Rev. B - *Condens. Matter Mater. Phys.* **1999**, *59* (3), 1758–1775. https://doi.org/10.1103/PhysRevB.59.1758.

(6) Togo, A.; Tanaka, I. First Principles Phonon Calculations in Materials Science. *Scr. Mater.* **2015**, *108*, 1–5. https://doi.org/10.1016/j.scriptamat.2015.07.021.

(7) Togo, A.; Chaput, L.; Tanaka, I. Distributions of Phonon Lifetimes in Brillouin Zones. *Phys. Rev. B* **2015**, *91*, 94306. https://doi.org/10.1103/PhysRevB.91.094306.

(8) A.J. Bard; Faulkner, L. R. Electrochemical Methods: Fundamentals and Applications; John Wiley & Sons, Inc.: New York, **2001**.

(9) Haram, S. K.; Kshirsagar, A.; Gujarathi, Y. D.; Ingole, P. P.; Nene, O. A.; Markad, G. B.; Nanavati, S. P. Quantum Confinement in CdTe Quantum Dots: Investigation through Cyclic Voltammetry Supported by Density Functional Theory (DFT). *J. Phys. Chem. C* **2011**, *115* (14), 6243–6249. https://doi.org/10.1021/jp111463f.

(10) Bae, Y.; Myung, N.; Bard, A. J. Electrochemistry and Electrogenerated Chemiluminescence of CdTe Nanoparticles. *Nano Lett.* **2004**, *4* (6), 1153–1161. https://doi.org/10.1021/nl049516x.

(11) Zhang, Z.; Shi, X.; Yang, X.; Fu, Y.; Zhang, K.; Lai, Y.; Li, J. Nanooctahedra Particles Assembled FeSe2 Microspheres Embedded into Sulfur-Doped Reduced Graphene Oxide Sheets As a Promising Anode for Sodium Ion Batteries. *ACS Appl. Mater. Interfaces* **2016**, *8* (22), 13849–13856. https://doi.org/10.1021/acsami.5b12148.

(12) Wang, H.; Wang, X.; Li, Q.; Li, H.; Xu, J.; Li, X.; Zhao, H.; Tang, Y.; Zhao, G.; Li, H.; Zhao, H.; Li, S. Constructing Three-Dimensional Porous Carbon Framework Embedded

with FeSe2 Nanoparticles as an Anode Material for Rechargeable Batteries. *ACS Appl. Mater. Interfaces* **2018**, *10* (45), 38862–38871. https://doi.org/10.1021/acsami.8b11479.

(13) Zhao, W.; Guo, C.; Li, C. M. Lychee-like FeS2@FeSe2 Core-Shell Microspheres Anode in Sodium Ion Batteries for Large Capacity and Ultralong Cycle Life. *J. Mater. Chem. A* **2017**, *5* (36), 19195–19202. https://doi.org/10.1039/c7ta05931k.

(14) Cho, J. S.; Lee, J.-K.; Kang, Y. C. Graphitic Carbon-Coated FeSe2 Hollow Nanosphere-Decorated Reduced Graphene Oxide Hybrid Nanofibers as an Efficient Anode Material for Sodium Ion Batteries. *Sci. Rep.* **2016**, *6* (1), 23699. https://doi.org/10.1038/srep23699.

(15) Zhang, K.; Hu, Z.; Liu, X.; Tao, Z.; Chen, J. FeSe2 Microspheres as a High-Performance Anode Material for Na-Ion Batteries. *Adv. Mater.* **2015**, *27* (21), 3305–3309. https://doi.org/10.1002/adma.201500196.

(16) He, P.; Yan, M.; Zhang, G.; Sun, R.; Chen, L.; An, Q.; Mai, L. Layered VS2 Nanosheet-Based Aqueous Zn Ion Battery Cathode. *Adv. Energy Mater.* **2017**, *7* (11), 1601920. https://doi.org/10.1002/aenm.201601920.

(17) Cao, L.; Gao, X.; Zhang, B.; Ou, X.; Zhang, J.; Luo, W. Bin. Bimetallic Sulfide Sb2S3@FeS2 Hollow Nanorods as High-Performance Anode Materials for Sodium-Ion Batteries. *ACS Appl. Mater. Interfaces* **2020**, *14*, 39. https://doi.org/10.1021/acsnano.0c00020.

(18) Cao, Z.; Chen, X.; Xing, L.; Liao, Y.; Xu, M.; Li, X.; Liu, X.; Li, W. Nano-MnO2@TiO2 Microspheres: A Novel Structure and Excellent Performance as Anode of Lithium-Ion Batteries. *J. Power Sources* **2018**, *379*, 174–181. https://doi.org/10.1016/j.jpowsour.2018.01.058.

(19) Kucur, E.; Riegler, J.; Urban, G. A.; Nann, T. Determination of Quantum Confinement in CdSe Nanocrystals by Cyclic Voltammetry. *J. Chem. Phys.* **2003**, *119* (4), 2333–2337. https://doi.org/10.1063/1.1582834.

(20) Fan, H.; Yu, H.; Zhang, Y.; Guo, J.; Wang, Z.; Wang, H.; Zhao, N.; Zheng, Y.; Du, C.; Dai, Z.; Yan, Q.; Xu, J. 1D to 3D Hierarchical Iron Selenide Hollow Nanocubes Assembled from FeSe2@C Core-Shell Nanorods for Advanced Sodium Ion Batteries. *Energy Storage Mater.* **2018**, *10*, 48–55. https://doi.org/10.1016/j.ensm.2017.08.006.

(21) Xu, J.; Jang, K.; Lee, J.; Kim, H. J.; Jeong, J.; Park, J. G.; Son, S. U. Phase-Selective Growth of Assembled FeSe2 Nanorods from Organometallic Polymers and Their Surface Magnetism. *Cryst. Growth Des.* **2011**, *11* (7), 2707–2710. https://doi.org/10.1021/cg2005562.

Chapter 5 Conclusions and Future Work

5.1 Conclusions

Semiconductor nano- or microscale particles have a high charging capacity in electrolyte systems. In order to further improve their capability, it is important to engineer particles with high surface corrugation and complex geometrical features to facilitate anomalous charge transport dynamics. The hedgehog particles introduced by the Kotov lab in recent years[1], in which a core particle is decorated by hundreds of high-aspect-ratio nanospikes, have increased surface corrugation and bring about a highly complex microparticle morphology. HPs possess a high dispersibility in various conditions including hydrophilic, hydrophobic, and even high ionic strength media, owing to their unique spiky structure which can drastically reduce the van der Waals forces between the particles to avoid coagulation in a large scale. Among all these HPs studied, $FeSe_2$ HPs synthesized in 2017[2] stood out as the most promising option for electrochemical studies due to the semiconductor properties of $FeSe_2$ (band gap of 0.6 – 1.0 eV from GGA calculations, by the collaborator Dr. Bingcheng Luo) and their structural integrity.

Herein, $FeSe_2$ HPs can potentially be applied as the active species in electrolyte systems. During the process of selecting the most suitable electrolyte system of $FeSe_2$ HPs, we conducted controlled experiments in different categories including changing the solvent (acetonitrile, *N,N*-dimethylformamide), the supporting electrolyte (lithium trifluoromethanesulfonate, tetrabutylammonium hexafluorophosphate, and tetrabutylammonium perchlorate), and the working electrode (glassy carbon, gold disk). We found that $FeSe_2$ HPs exhibited unique and

interesting electrochemical activities in the electrolyte system using DMF as a solvent, LiTf as a supporting electrolyte, and a gold disk as a working electrode.

This electrolyte system has high particle dispersibility and small resistance. CVs of $FeSe_2$ HPs display an oxidation peak at 0.65 V vs. Ag/Ag^+, with $FeSe_2$ HPs able to desorb from the surface of the working electrode after oxidation. Furthermore, this electrolyte system showed promising electrochemical and structural stability over the course of a long-term CV experiment, demonstrated by comparison of CV curves and SEM images before and after the CV test.

From bulk electrolysis experiments, $FeSe_2$ HPs were determined to have a large energy charging capacity in the magnitude of 10^8 charges per particle (or 0.7 positive charges per $FeSe_2$ crystalline unit cell) during oxidation, surpassing other nanoscale semiconductor materials when comparing charge per surface area, per volume and per crystal unit cell, potentially owing to HPs' high level of surface corrugation and complex geometry. Moreover, a comparison of charge per surface area of working electrode at peak potential indicated the great electrochemical activities of $FeSe_2$ HPs on the surface of gold disk working electrode. Finally, Fe and Se XPS spectra exhibited that mostly selenium atoms will be oxidized during the bulk electrolysis experiment.

5.2 Future Work

5.2.1 Iron Diselenide and its Energy-related Applications

$FeSe_2$ is a material being broadly investigated for a wide range of energy related applications including batteries[3,4] and electrocatalysis[5-15]. In the field of energy storage, the most notable is its application as an anode for sodium ion batteries, where it has demonstrated a large capacity (~500 mAh/g), long term cycling stability and high rate performance (~250 mAh/g at 10

A/g).[3] It will be of great interest if these excellent properties can be extended to the electrolyte systems of $FeSe_2$ HPs.

On the other hand, $FeSe_2$ has the potential to be applied as electrocatalysts.[14] Panda *et al.* synthesized a highly active $FeSe_2$ electrocatalyst for durable overall water splitting from a molecular 2Fe-2Se precursor. The as-synthesized $FeSe_2$ was electrophoretically deposited on nickel foam and applied to the oxygen and hydrogen evolution reactions (OER and HER, respectively) in alkaline media. When used as an oxygen-evolution electrode, a low 245 mV overpotential was achieved at a current density of 10 mA/cm^2, representing outstanding catalytic activity and stability because of $Fe(OH)_2$/FeOOH active sites formed at the surface of $FeSe_2$.[15] Kong *et al.* compared a couple of iron chalcogenides for HER, and $FeSe_2$ performed better than FeS_2 with a lower Tafel slope.[9] All of these results from benchmark electrocatalytic reactions can potentially predict a good electrocatalytic performance of $FeSe_2$ HPs.

5.2.2 $FeSe_2$ HPs as Electrocatalysts

Electrocatalysts are catalysts that can participate in electrochemical reactions. NP assemblies have been applied as electrocatalysts in various types of reactions for more than a decade. Due to relatively poor dispersibility in solvents, traditionally these electrocatalysts must be deposited on the surface of the electrode using solvents and binders. In this way, electrocatalysts are stably immobilized. Electrocatalytic reactions occur on the interfacial layer between electrocatalysts on the electrode (solid phase) and reactants in the solution (liquid phase). Therefore, the kinetics of traditional electrocatalytic reactions can be suppressed due to the limited surface area of electrodes. In other words, if the interfacial area between reactants and electrocatalysts is no longer confined to the small working electrode area, the speed of reactions

will be greatly improved. A feasible way to reach the goal is to disperse NP assemblies in electrolyte systems.

Based on previous studies[1,2,16-19], $FeSe_2$ HPs, a novel type of NP assemblies, can be well-dispersed in many solvents. Apart from the ability to be well-dispersed in solvents, in order to be an electrocatalyst, the electrochemical properties of $FeSe_2$ HPs need to be tested as well. As shown in this work, $FeSe_2$ HPs have displayed a high electrochemical stability in a wide voltage range.

In electrocatalytic reactions, electrocatalysts serve as a medium to transfer charges and drive the formation of products as a result. Therefore, ideal electrocatalysts should transfer as many charges as possible. NP and their assemblies usually contain thousands to millions of unit cells. One $FeSe_2$ HP contains an average of 2.2×10^8 units of $FeSe_2$ (section 4.3.1). Until now, the maximum number of charge passage per nanoparticle reported was *ca.* 270 electrons.[20] The lack of studies is due to the instability of traditional NP assemblies. However, in our case, owing to the improved electrochemical stability of $FeSe_2$ HPs, we reported a magnitude of 10^8 charge transfer capacity per $FeSe_2$ HP, which was the maximum number per NP assembly reported to date. This may be due to the ability of the lattice structure of $FeSe_2$ HPs to accommodate stress and remain stable within the plane during charge transfer.

It is reasonable to consider an electrocatalytic system with $FeSe_2$ electrocatalysts and reactants staying together in the liquid phase during catalytic reactions under electric fields. In this way, the interfacial area between reactants and electrocatalysts is no longer confined, and the speed of the reaction will be greatly improved. In the system containing small molecule homogeneous electrocatalysts[21,22] where electrocatalysts are present in the same phase (usually in the liquid phase) as reactants, $FeSe_2$ HPs can be compared to this system because they too are mobile and present in the liquid phase.

Practically, $FeSe_2$ HPs should still be considered as heterogeneous electrocatalysts since HPs do not really dissolve in solvents like the other small molecules do. However, these HPs can act like homogeneous electrocatalysts with the assistance of an electric field (Figure 5-1). Ideally, at the potential where $FeSe_2$ HPs are oxidized, the HPs are oxidized to $[FeSe_2\ HP]^{n+}$ and activate an electrocatalytic reaction to form the products from reactants. In facilitating the reaction, $[FeSe_2\ HP]^{n+}$ will be reduced, returning the starting catalyst material. In this way, HPs can be a charge shuttle to facilitate certain electrocatalytic reactions.

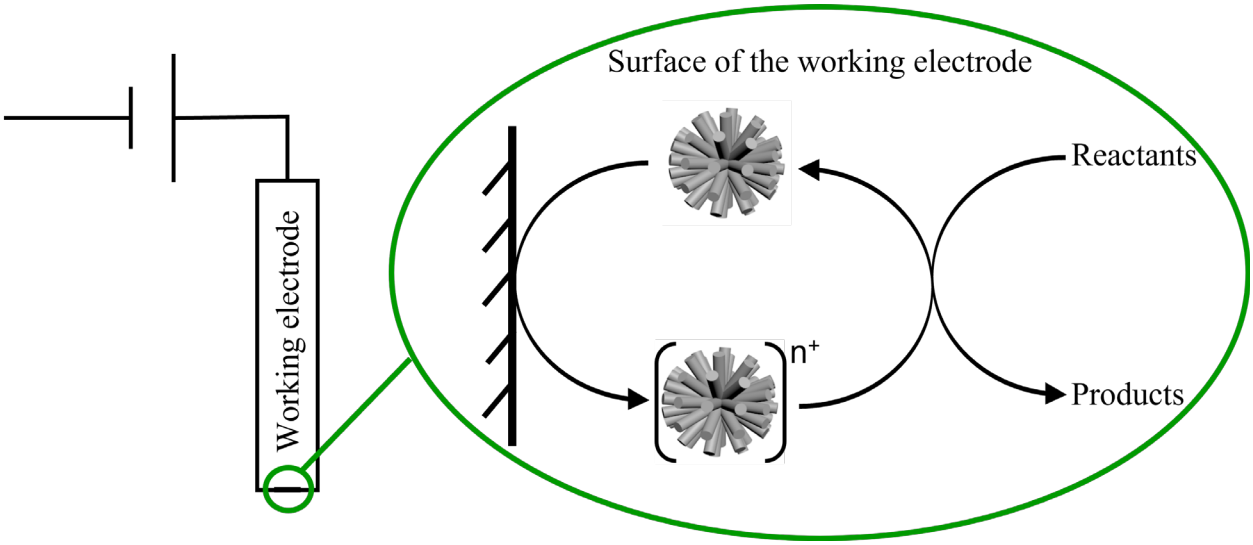

Figure 5-1 The diagram of a $FeSe_2$ HPs act like homogeneous electrocatalysts in heterogeneous electrocatalytic systems.

5.2.3 Selection of Electrocatalytic Reactions

Due to the high charging capacity demonstrated during the bulk oxidation of $FeSe_2$ HPs, an electrocatalytic oxidation reaction will be suitable for $FeSe_2$ HPs.

$FeSe_2$ NP assemblies have been demonstrated to be electrocatalysts for oxygen evolution reactions (OER).[5-8] OER is considered as a benchmark for electrocatalytic oxidation in aqueous systems. Although I did not consider water as the solvent due to possible correlation between the

value of the band gap and the value of the peak separation, potentially giving rise to incomplete electrochemical activities within the potential window of water, it does not necessarily mean that water cannot be considered especially with a peak separation of *ca.* 0.9 V in section 2.3.2. $FeSe_2$ had already demonstrated a good electrocatalytic activities of OER, so this test could validate the experimental setup of homogeneous-like heterogeneous electrocatalysts.

Considering the omni-dispersibility of $FeSe_2$ HPs especially in non-aqueous solvents, one can imagine to exploring electrocatalytic activities of HPs in non-aqueous systems. Currently, not a lot of electrocatalytic studies are done in systems with organic solvents. There are many challenges to face, including the solubility of reactants, the conductivity of the system, the stability of electrocatalysts, *etc.* There will be cost and safety concerns during scale-up. However, within the electrolyte system of $FeSe_2$ HP, many of these problems can potentially be solved. Therefore, it is worthwhile to apply HPs in many different non-aqueous electrocatalytic systems.

One of the most promising reactions for the application of $FeSe_2$ HPs is that of lignin degradation. Lignin constitutes ~20% of lignocellulosic biomass, as a byproduct in the pulp & paper industry and a waste material in the process of converting biomass to biofuel. Various degradative processes have been explored to break lignin down into compounds (chemical feedstocks) that can be either used in industry or completely degraded and removed from waste streams.[19,23] Our group has already reported that HPs with SiO_2 cores and ZnO nanospikes can facilitate and increase the yield in the photooxidation of 2-phenoxy-1-phenylethanol (a lignin model compound with a β-O-4 bond) to benzaldehyde and 2-phenoxyacetophenone by 6 and 35 times after optimization of HP geometry in high ionic strength conditions. It is believed that HP geometry not only reduces agglomeration but also modulates electric field effects at the solid−liquid interface. It is possible to tune the reaction pathway by changing the electrolyte

environment, modulating electrical fields at the spike−solvent interface mirroring field effects in electro- and piezocatalytic processes.[19] Therefore, the benefits of hedgehog structure may be further extended to electrocatalytic reactions in high ionic strength media.

5.2.4 Methodology of Electrocatalytic Studies Using $FeSe_2$ HPs

For the application of $FeSe_2$ HPs as electrocatalysts, one will use Linear Sweep Voltammetry (LSV) to test the performance of this electrocatalyst. As shown in Figure 5-2, the current increases when the potential is higher than the oxidation peak of $FeSe_2$ HPs. After that, the current will increase as the electrocatalytic reactions proceed. An electrocatalytic system with better electrocatalysts tends to have a larger current response and a smaller overpotential η (V, the potential difference between onset potential and potential to reach the benchmark current density of j = 10 mA cm^{-2}).

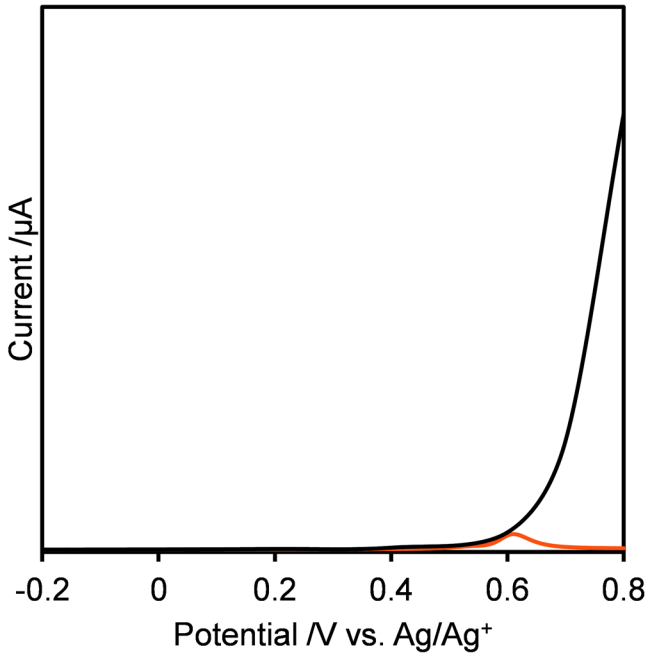

Figure 5-2 An expected LSV curve of an electrocatalytic system using $FeSe_2$ HPs as electrocatalysts.

Meanwhile, a chronopotentiometry test is another useful technique to show the stability of electrocatalyst activity. In chronopotentiometry, the current (density) is fixed, and the potentials (or overpotential) are measured over the course of the experiment to assess the stability of catalyst activity. One can compare LSV curves before and after the test to further prove the stability. After the measurement, the composition and structure of the electrocatalysts can be probed by SEM.

Apart from LSV and chronopotentiometry tests, some other previously applied electrochemical measurements can reveal more information. Nyquist plots obtained from EIS will give information about charge transfer resistance in the system (section 3.3.2). The smaller the charge transfer resistance is, the better the conductivity the electrolyte system has, and the better the catalytic activity of the electrocatalyst is. Furthermore, CVs within a narrow range without redox process can be applied to measure the double layer capacitance (C_d) to estimate the electrochemical active surface area (ECSA). A bigger capacitance represents a larger exposed electrochemically active surface area or catalytic active sites, benefitting from the high electrocatalyst–electrolyte contact interface area provided by the catalyst structure.

5.2.5 Originality, Contribution, and Significance to the Field

Many chemical reactions are closely related to our daily life. However, many of these reactions do not occur rapidly, requiring catalysts to drive them forward more quickly. Among different types of catalysts, electrocatalysts stimulate the reactions by applying easily-obtainable electric fields. The expansion of the electrocatalysis field has been severely hampered by the large bottleneck of a limited electrode surface area where catalytic reactions must occur. How can we break through this limitation?

One of the solutions is to apply homogeneous catalysts if electrocatalysts can be well-dispersed in an electrolyte systems with reactants. Currently, NP assemblies have not been widely applied in this field because most of them are unstable and difficult to disperse in liquid systems. Nevertheless, $FeSe_2$ HPs have the potential to become a pioneer in the application of NP assemblies as the next generation of "homogeneous" electrocatalysts owing to their omni-dispersibility in all solvents and excellent electrochemical properties including a large charging capacity demonstrated by both experimental and simulated results. If successful, this would be a major breakthrough in the field of electrocatalysis. The example of oxygen evolution reaction is just a starting point. Many other hedgehog-structured materials can be utilized for different types of electrocatalytic reactions.[24-26] Moreover, other structured NP assemblies which are chemically and electrochemically stable will potentially serve as good candidates of dispersed heterogeneous electrocatalysts as well. In this way, there can be endless combinations of homogeneous-like heterogeneous electrocatalysts and corresponding electrochemical reactions in the field of catalysis.

5.3 References

(1) Bahng, J. H.; Yeom, B.; Wang, Y.; Tung, S. O.; Hoff, J. D.; Kotov, N. Anomalous Dispersions of "hedgehog" Particles. *Nature* **2015**, *517* (7536), 596–599. https://doi.org/10.1038/nature14092.

(2) Deng, D.; Hao, C.; Sen, S.; Xu, C.; Král, P.; Kotov, N. A. Template-Free Hierarchical Self-Assembly of Iron Diselenide Nanoparticles into Mesoscale Hedgehogs. *J. Am. Chem. Soc.* **2017**, *139* (46), 16630–16639. https://doi.org/10.1021/jacs.7b07838.

(3) Zhao, F.; Shen, S.; Cheng, L.; Ma, L.; Zhou, J.; Ye, H.; Han, N.; Wu, T.; Li, Y.; Lu, J. Improved Sodium-Ion Storage Performance of Ultrasmall Iron Selenide Nanoparticles. *Nano Lett.* **2017**, *17* (7), 4137–4142. https://doi.org/10.1021/acs.nanolett.7b00915.

(4) Zhang, K.; Hu, Z.; Liu, X.; Tao, Z.; Chen, J. FeSe2 Microspheres as a High-Performance Anode Material for Na-Ion Batteries. *Adv. Mater.* **2015**, *27* (21), 3305–3309. https://doi.org/10.1002/adma.201500196.

(5) Gao, R.; Zhang, H.; Yan, D. Iron Diselenide Nanoplatelets: Stable and Efficient Water-Electrolysis Catalysts. *Nano Energy* **2017**, *31*, 90–95. https://doi.org/10.1016/J.NANOEN.2016.11.021.

(6) Yang, Z.; Zhang, J.-Y.; Liu, Z.; Li, Z.; Lv, L.; Ao, X.; Tian, Y.; Zhang, Y.; Jiang, J.; Wang, C. "Cuju"-Structured Iron Diselenide-Derived Oxide: A Highly Efficient Electrocatalyst for Water Oxidation. *ACS Appl. Mater. Interfaces* **2017**, *9* (46), 40351–40359. https://doi.org/10.1021/acsami.7b14072.

(7) Nai, J.; Lu, Y.; Yu, L.; Wang, X.; Lou, X. W. D. Formation of Ni-Fe Mixed Diselenide Nanocages as a Superior Oxygen Evolution Electrocatalyst. *Adv. Mater.* **2017**, *29* (41), 1703870. https://doi.org/10.1002/adma.201703870.

(8) Xu, X.; Song, F.; Hu, X. A Nickel Iron Diselenide-Derived Efficient Oxygen-Evolution Catalyst. *Nat. Commun.* **2016**, *7*. https://doi.org/10.1038/ncomms12324.

(9) Kong, D.; Cha, J. J.; Wang, H.; Lee, H. R.; Cui, Y. First-Row Transition Metal Dichalcogenide Catalysts for Hydrogen Evolution Reaction. *Energy Environ. Sci.* **2013**, *6* (12), 3553–3558. https://doi.org/10.1039/c3ee42413h.

(10) Shwetharani, R.; Nagaraju, D. H.; Geetha Balakrishna, R.; Suvina, V. Hydrogenase Enzyme like Nanocatalysts FeS 2 and FeSe 2 for Molecular Hydrogen Evolution Reaction. *Mater. Lett.* **2019**, *248*, 39–42. https://doi.org/10.1016/j.matlet.2019.03.131.

(11) Xu, X.; Ge, Y.; Wang, M.; Zhang, Z.; Dong, P.; Baines, R.; Ye, M.; Shen, J. Cobalt-Doped FeSe2-RGO as Highly Active and Stable Electrocatalysts for Hydrogen Evolution Reactions. *ACS Appl. Mater. Interfaces* **2016**, *8* (28), 18036–18042. https://doi.org/10.1021/acsami.6b03849.

(12) Guan, Y.; Feng, Y.; Mu, Y.; Zhang, H.; Wang, Y. Controlled Synthesis of Unique Porous FeSe2 Nanomesh Arrays towards Efficient Hydrogen Evolution Reaction. *Electrochim. Acta* **2017**, *247*, 435–442. https://doi.org/10.1016/j.electacta.2017.07.039.

(13) Zhang, J.; Tian, P.; Tang, T.; Huang, G.; Zeng, J.; Cui, B.; Shen, Z.; Wang, H.; Kong, Z.; Xi, J.; Ji, Z. Excellent Photoelectrochemical Hydrogen Evolution Performance of FeSe2 Nanorod/ZnSe 0D/1D Heterostructure as Efficiency Carriers Migrate Channel. *Int. J. Hydrogen Energy* **2020**, *45* (15), 8526–8539. https://doi.org/10.1016/j.ijhydene.2020.01.051.

(14) Hou, B.; Benito-Alifonso, D.; Webster, R. F.; Cherns, D.; Galan, M. C.; Fermín, D. J. Synthetic Mechanism Studies of Iron Selenides: An Emerging Class of Materials for Electrocatalysis. *Catalysts* **2021**, *11* (6), 1 – 15. https://doi.org/10.3390/catal11060681.

(15) Panda, C.; Menezes, P. W.; Walter, C.; Yao, S.; Miehlich, M. E.; Gutkin, V.; Meyer, K.; Driess, M. From a Molecular 2Fe-2Se Precursor to a Highly Efficient Iron Diselenide Electrocatalyst for Overall Water Splitting. *Angew. Chemie Int. Ed.* **2017**, *56* (35), 10506–10510. https://doi.org/10.1002/anie.201706196.

(16) Montjoy, D. G.; Bahng, J. H.; Eskafi, A.; Hou, H.; Kotov, N. A. Omnidispersible Hedgehog Particles with Multilayer Coatings for Multiplexed Biosensing. *J. Am. Chem. Soc.* **2018**, *140* (25), 7835–7845. https://doi.org/10.1021/jacs.8b02666.

(17) Kirchner, S. R.; Su, M. N.; Bahng, J. H.; Montjoy, D. G.; Chang, W. S.; Kotov, N.; Link, S. Scattering Properties of Individual Hedgehog Particles. *J. Phys. Chem. C* **2018**, *122* (22), 12015–12021. https://doi.org/10.1021/acs.jpcc.8b03823.

(18) Montjoy, D. G.; Hou, H.; Bahng, J. H.; Kotov, N. A. Omnidispersible Microscale Colloids with Nanoscale Polymeric Spikes. *Chem. Mater.* **2020**, *32* (23), 9897–9905. https://doi.org/10.1021/acs.chemmater.0c02472.

(19) Montjoy, D. G.; Hou, H.; Bahng, J. H.; Eskafi, A.; Jiang, R.; Kotov, N. A. Photocatalytic Hedgehog Particles for High Ionic Strength Environments. *ACS Nano* **2021**, *15* (3), 4226–4234. https://doi.org/10.1021/acsnano.0c05992.

(20) Albery, W. J.; Bartlett, P. N.; Porter, J. D. The Electrochemistry of Colloidal Semiconductor Particles: Experiments on CdS and TiO2. *J. Electrochem. Soc.* **1984**, *131* (12), 2896–2900. https://doi.org/10.1149/1.2115438.

(21) Siu, J. C.; Fu, N.; Lin, S. Catalyzing Electrosynthesis: A Homogeneous Electrocatalytic Approach to Reaction Discovery. *Acc. Chem. Res.* **2020**, *53* (3), 547–560. https://doi.org/10.1021/acs.accounts.9b00529.

(22) Zhang, S.; Fan, Q.; Xia, R.; Meyer, T. J. CO2 Reduction: From Homogeneous to Heterogeneous Electrocatalysis. *Acc. Chem. Res.* **2020**, *53* (1), 255–264. https://doi.org/10.1021/acs.accounts.9b00496.

(23) Chang, X.; van der Zalm, J.; Thind, S. S.; Chen, A. Electrochemical Oxidation of Lignin at Electrochemically Reduced TiO2 Nanotubes. *J. Electroanal. Chem.* **2020**, *863*, 114049. https://doi.org/10.1016/j.jelechem.2020.114049.

(24) Liu, Y.; Guo, R.; Duan, C.; Wu, G.; Miao, Y.; Gu, J.; Pan, W. A Highly Effective Urchin-like MnCrOx Catalyst for the Selective Catalytic Reduction of NOx with NH3. *Fuel* **2020**, *271*, 117667. https://doi.org/10.1016/j.fuel.2020.117667.

(25) Chen, Y.; Niu, H. J.; Feng, Y. G.; Wu, J. H.; Wang, A. J.; Huang, H.; Feng, J. J. Three-Dimensional Hierarchical Urchin-like PdCuPt Nanoassembles with Zigzag Branches: A Highly Efficient and Durable Electrocatalyst for Formic Acid Oxidation Reaction. *Appl. Surf. Sci*. **2020**, *510*, 145480. https://doi.org/10.1016/j.apsusc.2020.145480.

(26) Dong, F.; Guo, Y.; Zhang, D.; Zhu, B.; Huang, W.; Zhang, S. Gold Nanoparticles Supported on Urchin-Like CuO: Synthesis, Characterization, and Their Catalytic Performance for CO Oxidation. *Nanomaterials* **2019**, *10* (1), 67. https://doi.org/10.3390/nano10010067.